A STUDY ON THE ESTIMATION OF SCATTERING CROSS SECTION–MASS BOUND FOR COLD DARK MATTER MODEL USING DIFFUSE RADIO EMISSION FROM GALAXY CLUSTERS

KIEW CHING YEE

FACULTY OF SCIENCE
UNIVERSITY OF MALAYA
KUALA LUMPUR

2018

A STUDY ON THE ESTIMATION OF SCATTERING CROSS SECTION–MASS BOUND FOR COLD DARK MATTER MODEL USING DIFFUSE RADIO EMISSION FROM GALAXY CLUSTERS

KIEW CHING YEE

DISSERTATION SUBMITTED IN FULFILMENT OF THE REQUIREMENTS FOR THE DEGREE OF MASTER OF SCIENCE

DEPARTMENT OF PHYSICS
FACULTY OF SCIENCE
UNIVERSITY OF MALAYA
KUALA LUMPUR

2018

UNIVERSITY OF MALAYA

ORIGINAL LITERARY WORK DECLARATION

Name of Candidate: **KIEW CHING YEE**

Matric No.: **SGR140064**

Name of Degree: **MASTER OF SCIENCE**

Title of Project Paper/Research Report/Dissertation/Thesis ("this Work"):

A STUDY ON THE ESTIMATION OF SCATTERING CROSS SECTION–MASS BOUND FOR COLD DARK MATTER MODEL USING DIFFUSE RADIO EMISSION FROM GALAXY CLUSTERS

Field of Study: **THEORETICAL PHYSICS**

I do solemnly and sincerely declare that:

(1) I am the sole author/writer of this Work;
(2) This Work is original;
(3) Any use of any work in which copyright exists was done by way of fair dealing and for permitted purposes and any excerpt or extract from, or reference to or reproduction of any copyright work has been disclosed expressly and sufficiently and the title of the Work and its authorship have been acknowledged in this Work;
(4) I do not have any actual knowledge nor do I ought reasonably to know that the making of this work constitutes an infringement of any copyright work;
(5) I hereby assign all and every rights in the copyright to this Work to the University of Malaya ("UM"), who henceforth shall be owner of the copyright in this Work and that any reproduction or use in any form or by any means whatsoever is prohibited without the written consent of UM having been first had and obtained;
(6) I am fully aware that if in the course of making this Work I have infringed any copyright whether intentionally or otherwise, I may be subject to legal action or any other action as may be determined by UM.

Candidate's Signature Date:

Subscribed and solemnly declared before,

Witness's Signature Date:

Name:

Designation:

A STUDY ON THE ESTIMATION OF SCATTERING CROSS SECTION–MASS BOUND FOR COLD DARK MATTER MODEL USING DIFFUSE RADIO EMISSION FROM GALAXY CLUSTERS

ABSTRACT

Galaxy clusters are the largest gravitationally bounded systems in the Universe. Approximately 80% of mass in the galaxy clusters are in the form of dark matter. Although dark matter has been proven to exist, its nature is still a mystery. The neutralino from supersymmetry theory is one of the favourite candidate for dark matter. If neutralino is the main composition of dark matter, their self-annihilation can result in synchrotron emission in galaxy clusters. On the other hand, diffuse radio emissions (e.g., radio halos, mini halos, and radio relics) are found in a small fraction of galaxy clusters. By assuming the dark matter to be composed of neutralinos, the expected synchrotron emission from the dark matter neutralinos in galaxy clusters was estimated. The constraint on the properties of neutralino was set by using the diffuse radio emission from galaxy clusters. The results showed the upper limit constraint on $\langle\sigma v\rangle$–m_χ space with neutralino annihilates through different channels. The uncertainties on the constraint due to the dark matter density profile and cluster magnetic field were identified. The thesis also investigated the neutralino from minimial SUperGRAvity (mSUGRA) and Minimal Supersymmetric Standard Model (MSSM) models. The results showed that the neutralino can contribute partly to the diffuse radio emission, whereas the amount of which depends on the supersymmetric model adopted.

Keywords: Elementary particles, radiation mechanisms: non-thermal, galaxies: clusters, dark matter.

KAJIAN UNTUK MENGANGGAR HAD KEKANGAN PADA KERATAN RENTAS–JISIM BAGI MODEL JIRIM GELAP SEJUK DENGAN MENGGUNAKAN PANCARAN RADIO TERBAUR DARI GUGUSAN GALAKSI

ABSTRAK

Gugusan galaksi adalah sistem graviti terikat yang terbesar dalam alam semesta. Dianggarkan 80% jisim yang dalam gugusan galaksi ialah jirim gelap. Walaupun jirim gelap telah terbukti wujud, sifatnya masih adalah misteri. Neutralino dari teori 'supersymmetry' ialah salah satu calon kegemaran untuk jirim gelap. Sekiranya neutralino adalah komposisi utama jirim gelap, penghapusan diri neutralino boleh menyebabkan pelepasan radiasi sinkrotron dari gugusan galaksi. Sementara itu, terdapat pancaran radio tarbaur (contohnya, halo radio, halo mini, dan tinggalan radio) dalam sebahagian kecil daripada gugusan galaksi. Dengan menganggap jirim gelap terdiri daripada neutralino, pelepasan radiasi sinkrotron dari jirim gelap telah ditaksir dalam tesis ini. Kekangan kepada sifat-sifat neutralino juga telah ditetapkan dengan menggunakan pancaran radio terbaur dari gugusan galaksi. Hasil kajian tesis ini menunjukkan had kekangan atas pada $\langle\sigma v\rangle$–m_χ dengan menganggap bahawa neutralino menghapuskan diri melalui saluran yang berbeza. Ketidakpastian mengenai kekangan yang disebabkan oleh profil ketumpatan jirim gelap dan medan magnet gugusan galaksi telah ditetapkan. Tesis ini juga menyiasat neutralino dari model minimial SUperGRAvity (mSUGRA) dan Minimal Supersymmetric Standard Model (MSSM). Hasil kajian ini menunjukkan bahawa neutralino boleh menyumbang kepada sebahagian pancaran radio terbaur, manakala jumlahnya bergantung kepada model 'supersymmetry' yang digunakan.

Kata kunci: Zarah asas – mekanisme radiasi: non-terma – gugusan galaksi – jirim gelap.

ACKNOWLEDGEMENTS

First of all, I would like to express my very great appreciation to Assoc. Prof. Dr. Zamri Zainal Abidin and Prof. Chorng-Yuan Hwang for giving me their patience, motivation, and immense knowledge throughout my study. I wouldn't have achieved this without your guidance! I would also like to offer my very sincere and special thanks to Graduate Institute of Astronomy, National Central University, Taiwan, from which I gained an enormous amount of knowledge and a wonderful experience. A big thank you to my fellow labmates in Radio Cosmology Research Group and Dr. Chrisphin Karthick, for their support from various aspects, sharing of knowledge, and entertaining discussions. Most importantly, I would like express my deep gratitude to Yong Hong and my beloved family members for their love, understanding, and encouragement to me. Bagus!

TABLE OF CONTENTS

LIST OF FIGURES

LIST OF TABLES

LIST OF SYMBOLS AND ABBREVIATIONS

$B^{(1)}$	:	first KK excitation of hypercharge gauge boson.
B_0	:	central magnetic field.
D_L	:	luminosity distance.
H_0	:	Hubble's constant at present day $= 100\ h$ km s^{-1} Mpc^{-1}.
M_{vir}	:	virial mass.
Q_e	:	electron source spectrum.
S_ν	:	radio flux density.
ΛCDM	:	Lambda cold dark matter model.
χ	:	dark matter particle.
ϵ_ν	:	synchrotron radiation emissivity.
η	:	proportional index of magnetic field to the intra-cluster gas density.
γ	:	Lorentz factor.
$\langle\sigma v\rangle$	:	thermally averaged annihilation cross section.
$\mathrm{M}_\odot$	:	solar mass $= 1.99 \times 10^{30}$ kg.
ρ_{crit}	:	critical density of the universe.
Ω_Λ	:	density parameter of dark energy = 0.7.
Ω_m	:	density parameter of massive matter = 0.3.
b	:	energy loss through radiations.
c	:	speed of light $= 3.0 \times 10^8$ m s^{-1}.
c_{vir}	:	virial concentration.
e	:	elementary charge $= 1.602 \times 10^{-19}$ C.
h	:	hubble parameter = 0.7.
m_e	:	electron mass $= 9.109 \times 10^{-31}$ kg.
n_{eq}	:	electron equilibrium spectrum.

n_{gas}	:	intracluster gas density.
r_c	:	core radius.
z	:	redshift.
$\frac{dN}{dE}$	:	electron energy spectrum.
ADD	:	large extra dimension.
AGN	:	active galactic nucleus.
BCG	:	brightest cluster galaxy.
BR	:	branching ratio.
CM	:	caustic method.
CMB	:	cosmic microwave background.
GUT	:	Grand Unified Theory.
ICM	:	intracluster medium.
KK	:	Kaluza-Klein.
l.o.s.	:	line-of-sight.
LAT	:	Large Area Telescope.
LHC	:	Large Hadron Collider.
LKP	:	lightest Kaluza-Klein particle.
LOSVD	:	line-of-sight velocity dispersion.
LSP	:	lightest supersymmetric particle.
MACHO	:	massive astrophysical compact halo object.
MSSM	:	Minimal Supersymmetric Standard Model.
mSUGRA	:	minimial SUperGRAvity.
NFW	:	Navarro-Frenk-White.
SM	:	Standard Model of particle physics.
SUSY	:	Supersymmetry.
UED	:	universal extra dimension.
VLBI	:	Very-Long-Baseline Interferometry.

WIMP : weakly interacting massive particle.

LIST OF APPENDICES

CHAPTER 1: INTRODUCTION

1.1 Research Questions

It is well-known that the Standard Model of particle physics (SM) is a very successful theory. It describes the interaction between the fundamental building blocks of matter and the fundamental forces. However, it is not perfect. There are a few phenomena that it could not explain, e.g., the gravity, the mass of neutrino, the matter–antimatter asymmetry in universe, the dark matter and dark energy from cosmological observations, and etc. The dark matter is one of the most puzzling questions in both physics and astronomy. The dark matter is massive and dominates the matter component of universe. Its existence is proved by many compelling astronomical observations, but none is known about its nature. The existence of such hypothetical matter would solve a number of puzzling questions observed in astronomy, e.g., the flatness of galactic rotation curve, the discrepancy between the luminous mass and dynamical mass in galaxies and galaxy clusters, the formation of large scale structure of the universe and etc. Many new particles from physics beyond the SM are proposed as the dark matter candidate, but none of them are detected and confirmed.

The weakly interacting massive particle (WIMP) is one of the most favourable dark matter candidate. If WIMP is the only type of particle that composites the dark matter and majority of the galaxy cluster mass, under the environment of cluster-wide magnetic field, the electrons and positrons (produced as one of the various WIMP pair-annihilation products) are accelerated and emit synchrotron emission. On the other hand, some galaxy clusters in radio band show large scale diffuse radio emission (in particular, the radio halo) with no optical counterpart. The origin of this radio halo is still unclear. It is possible that the charged particles from WIMP annihilation eventually lead to the production of diffuse

radio emission. In fact, this is central idea on which this research is based. This study interprets the radio halo as one of the end results of WIMP annihilation.

1.2 Motivation

The origin of diffuse radio emission and the dark matter are still open questions. The search for dark matter needs to be done from many aspects, i.e., the direct detection, indirect detection, and collider experiment, as each aspect provides a different piece of information to complete the puzzle. This study aims to approach the dark matter problem from the aspect of radio observation, at the same time investigate the relation between the dark matter and the diffuse radio emission. The single dish radio telescope built by University of Malaya (in conjunction with the Sultan Idris Education University) is expected to play an important role in this research in future: The future Very-Long-Baseline Interferometry (VLBI) network between this telescope and the neighbouring countries is expected to provide a high resolution observation to the discrete radio sources in a galaxy cluster; while the single dish radio telescope itself recovers the flux missed by the interferometer.

1.3 Objective

The objectives of this research are highlighted as follows.

1. To study the interaction between particle physics and cosmology to understand dark matters.

2. To set constraints on the properties of dark matter candidate by using the diffuse radio emission from galaxy clusters.

3. To estimate the bound on the dark matter annihilation cross section–mass relation.

1.4 Thesis Flow

This thesis is structured as follows: the current researches on the dark matter and diffuse radio emission are reviewed in Chapter 2. The steps to derive the synchrotron emission from dark matter are described in details in Chapter 3. Results are shown and discussed in Chapter 4. Chapter 5 summarizes the research and conclusions.

CHAPTER 2: LITERATURE REVIEW

2.1 Evolution of the Universe

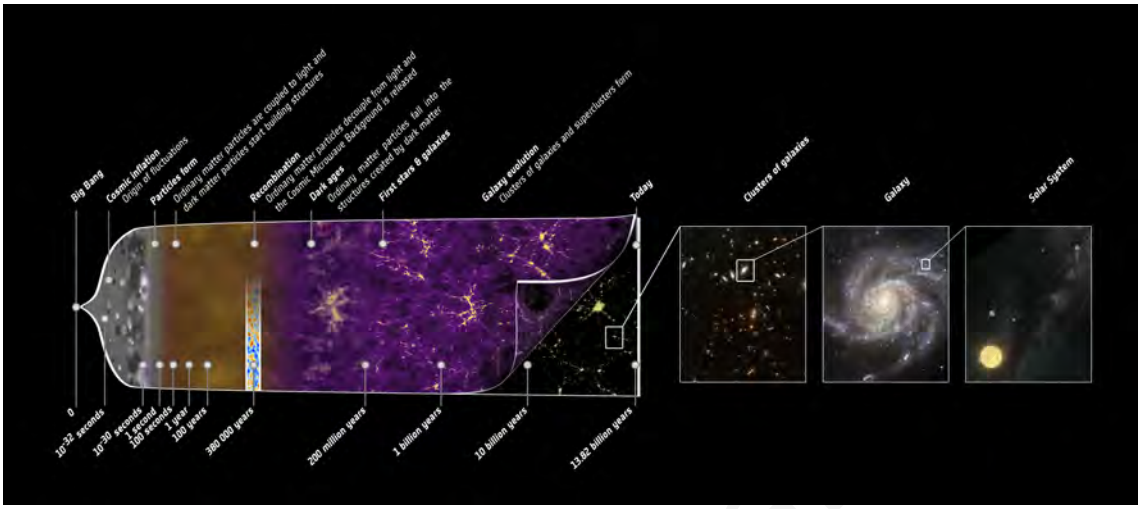

Figure 2.1: Evolution of the universe over 13.8 billion years (Image credit: ESA–C. Carreau).

In the early 1900s, it was revealed that the objects in the universe are moving away from each other (Slipher, 1917; Hubble, 1929); the object's distance and radial velocity follow a linear relationship that is now called the Hubble's law. This discovery implies the expansion of universe. The singular point from which the expansion first started is called the Big Bang. It happened around 13.8 billion years ago. In the time less than 10^{-32} second after the Big Bang, the universe underwent the inflationary epoch – an accelerated expansion of space. During the inflation, the quantum fluctuations were magnified to astrophysical scale, and formed the seeds for large scale structure formation. The inflation is responsible for producing a spatially-flat, homogeneous, and isotropic universe on large scale.

After the inflation, the universe entered the radiation-dominated era and the expansion continues in a lower rate. Under the high temperature environment, the elementary particles were continuously paired-produced and annihilated. As the expansion continues, the universe cooled down and hadrons started to form, and eventually the atomic nuclei. The universe was then filled with the hot plasma that consisted of nuclei, electrons, and photons.

The plasma was so hot that the particles kept interacting with the photons, and no photon could escape as free radiation.

Eventually the universe cooled down to a point where the temperature is low enough for the neutral hydrogen atoms to form. Therefore, the particles interact much less with the photons, the photons could now escape and travel freely through space. The photons that survive until today are observed as the cosmic microwave background (CMB). The CMB photons observed today have been redshifted during its travel through the expanding space. Measurement shows that the current CMB is an extremely low temperature radiation that corresponds to a blackbody of 2.7255 K (Fixsen, 2009).

The current cosmological model describes the universe as composed of dark energy, matter, and radiation. The temperature variation of CMB over the sky gives information about the universe, e.g., curvature of the universe, baryon density, matter density, and etc. The Planck measurement on the CMB anisotropies shows that 69.2% of the energy–mass density of the universe is in the form of dark energy, 25.8% as dark matter, and 4.8% as baryonic matter (Planck Collaboration, 2016). The densities of the three components are usually written in the form of density parameter, $\Omega_i(z) \equiv \rho_i(z)/\rho_{crit}(z)$, where ρ_i denotes the density of i component, z is the redshift, and ρ_{crit} is known as the critical density of the universe. The critical density is the total density of the universe at which the universe is flat (neither closed nor open). For an 'open' universe ($\rho_{total} < \rho_{crit}$), the expansion will continue forever; for a 'closed' universe ($\rho_{total} > \rho_{crit}$), the expansion will halt someday, leading to the collapse of universe; while for a 'flat' universe ($\rho_{total} = \rho_{crit}$), the expansion gradually slows down, and will only stop in the infinite future. The current measurement strongly favours a flat universe.

During the expansion of the universe, the energy density of the radiation fell faster than that of the matter. The energy density of matter eventually surpassed that of the

radiation, the universe entered the matter-dominated era. In the matter-dominated era, the dark matter perturbation grew under the influence of gravity. This overdensity attracted the nearby matter. Over time, it grew denser and the structure of universe formed hierarchically (bottom-up): the smaller structure formed first and merged with others to form a larger structure. The current universe is in the dark energy dominated era according to measurements (Bennett et al., 2013; Planck Collaboration, 2016).

One of the categorizations of dark matter classifies the dark matter into two types: the cold (non-relativistic) and hot (relativistic) dark matter. A cold-dark-matter-dominated scenario would allow the early formation of the first galaxy and the formation of fine structure. If the matter component is dominated by the hot dark matter instead, the dark matter particles would move rapidly and tend to wash out the small scale fluctuations in the matter distribution. In this scenario, the universe structure would form by fragmentation (top-down), where the largest structures form first, and then subdividing into clusters, groups, and galaxies. Without the introduction of cold dark matter, the galaxies and superclusters would form at a relatively late time. However, the detection of the oldest galaxy ($z \approx 10$) favours the cold dark matter scenario. In fact, the currently accepted standard model of cosmology is referred to as Lambda cold dark matter model (ΛCDM), as it embraces the cold dark matter (and the cosmological constant Λ that is associated with the dark energy).

2.2 Evidence of Dark Matter

Up until today, all the evidence about the existence of the dark matter are only inferred by its gravitational interaction with the surroundings.

The existence of dark matter was first noticed by Fritz Zwicky in 1933, where he found that the average mass density in the Coma cluster inferred by its observed velocity dispersion is 400 times higher than that inferred by only the luminous matter (Zwicky,

1933). Besides the velocity dispersion of cluster members, the distortion of the images of the background galaxies by the massive foreground cluster (which is the gravitational lensing effect) also points to the existence of dark matter. Another evidence to the dark matter on the cluster scale is the X-ray emitting hot gas: In a galaxy cluster, the intracluster gas is held by a strong gravity; in order to counterbalance the strong gravitational pressure, the hot plasma has to be in high temperature (few keV) and emits in X-ray. On the galaxy scale, the most direct evidence of the dark matter is the flatness of the galactic rotation curve (van Albada et al., 1985).

2.3 Dark Matter Candidate

Despite the evidence that proves the existence of dark matter, no dark matter has been directly detected and its properties is yet to be confirmed. From the astronomy point of view, it is possible that the dark matter consists of not only one type of particles. Nevertheless, the cold and non-baryonic dark matter must take up the majority. There are some characteristics that a dark matter particle must fulfil. It has to be

- non-baryonic: According to the Planck measurement on the CMB, majority of the matter are in the form of non-baryonic matter. This rules out the protons and neutrons as the main dark matter component;
- cold: Majority of the dark matter must move non-relativistically in order to form the large scale structure of universe, ruling out the light neutrinos as the main dark matter;
- dark: Dark matter does not interact with the electromagnetic radiation, making them invisible to telescopes. All the charged leptons are therefore ruled out as dark matter candidate; and

- stable: The dark matter must be stable on cosmological time scale (it does not decay, but it is allowed to annihilate with its antiparticle). This rules out W, Z, and Higgs bosons as dark matter.

None of the SM particles fulfil all the criteria as dark matter. The dark matter must be some new particles beyond the SM. Some of the promising dark matter candidates are listed below.

(a) ***Axions.***

Axion was first proposed to solve the problem of CP violation in QCD (Peccei & Quinn, 1977; Weinberg, 1978; Wilczek, 1978). Axions are light but slow-moving particles. There is a mass window (micro eV range) that will leave them the right relic abundance of dark matter, since they are produced non-thermally.

(b) ***Sterile neutrinos.***

Sterile neutrinos are right-handed neutrinos. They are even less interactive than the active neutrinos in SM. A sterile neutrino in keV mass can constitute dark matter.

(c) ***Massive astrophysical compact halo objects (MACHOs).***

MACHOs are ordinary matters. They emit very little or no electromagnetic radiation, making them hard to detect. Examples of MACHOs are the neutron stars, brown and white dwarfs, non-luminous planets, black holes, and etc. However, since the CMB results told us that majority of the dark matter are in the form of non-baryonic matter, MACHOs itself cannot be the primary composition of dark matter.

(d) ***WIMPs.***

WIMP is a category of elementary particles that are massive (≈10 GeV to a few TeV) and interact 'weakly' with the electroweak gauge bosons and Higgs boson. They also

interact via gravitational force. Examples of WIMPs are the lightest supersymmetric particle (LSP), the lightest Kaluza-Klein particle (LKP), the heavy neutrinos, and etc. The relic abundance of WIMPs can be related to its annihilation cross section through the following process. When the universe cools to the temperature below the WIMP mass, the creation of WIMPs drops exponentially. At the same time, the drop in WIMP density caused by the expansion lowers the chances for one WIMP to meet and annihilate with another. The WIMPs therefore "freeze-out", its abundance remains constant and is left as relic density today. The relic abundance of WIMP today can be approximately related to its thermally averaged annihilation cross section ($\langle \sigma v \rangle$) through the relation below (Jungman et al., 1996):

$$\Omega_\chi h^2 \simeq \frac{3 \times 10^{-27}\ \mathrm{cm}^3\ \mathrm{s}^{-1}}{\langle \sigma v \rangle}, \tag{2.1}$$

where Ω_χ denotes the density parameter of dark matter, and h denotes the Hubble parameter. The interaction cross section of WIMP happens to fall in the range that accounts for the right relic abundance of dark matter, which makes WIMP a good dark matter candidate. This is called the WIMP miracle.

This study focused on the WIMPs (more specifically, the LSP and LKP). These two candidates are briefly introduced in the following section.

2.3.1 Supersymmetric Neutralino

The neutralino is a hypothetical particle predicted by the Supersymmetry (SUSY) theory. Supersymmetry theory was first proposed to solve the hierarchy problem in physics. In the SM, electromagnetic and weak forces are unified into a single force called electroweak force at high energy (> 246 GeV). It is natural for one to seek for an even higher energy scale at which the electroweak and strong forces unify. This is expected to happen at the Grand

Unified Theory (GUT) scale ($\approx 10^{16}$ GeV). However, with only the current SM theory, the three forces fail to unify. Moreover, the huge order of difference between the electroweak symmetry breaking scale and GUT symmetry breaking scale would give an enormous quantum correction to Higgs mass, pushing it to around the order of GUT scale (or Planck scale $\approx 10^{18}$ GeV) if that is really the fundamental scale of physics. However, the mass of Higgs boson was experimentally discovered to be only $\approx$ 125 GeV. One way to solve this problem is by introducing a superpartner with spin differed by one half to all the SM particles (while all other quantum numbers remain the same). The cancellation between the bosonic and fermionic contributions reduces the quantum correction, protecting the Higgs from mass divergence. This is called the Supersymmetry theory. SUSY is also able to predict the convergence of the three fundamental forces at GUT scale, which is unable to be achieved by only the SM. In a nutshell, SUSY allows the huge order of difference between the electroweak and GUT symmetry breaking scales, at the same time not driving up the Higgs mass.

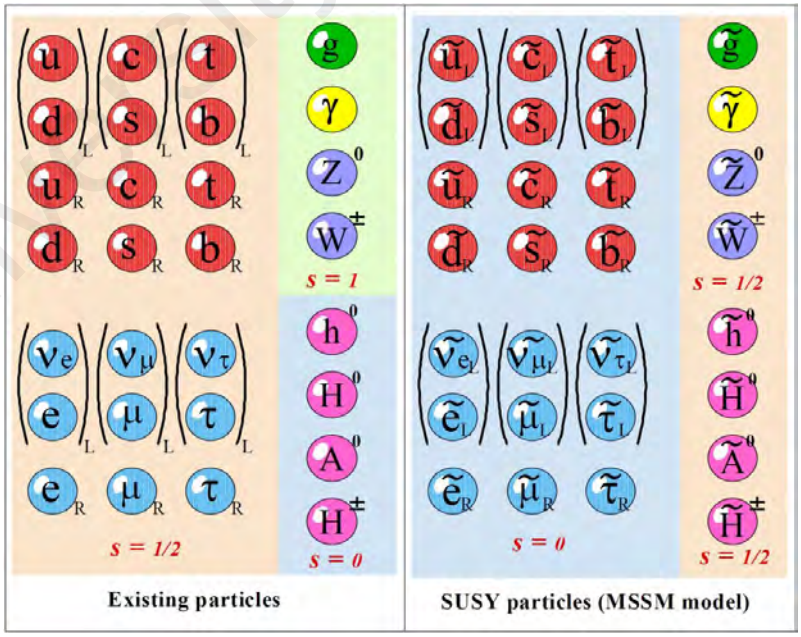

Figure 2.2: SM particles and their superpartners (Image credit: KEK, High Energy Accelerator Research Organization).

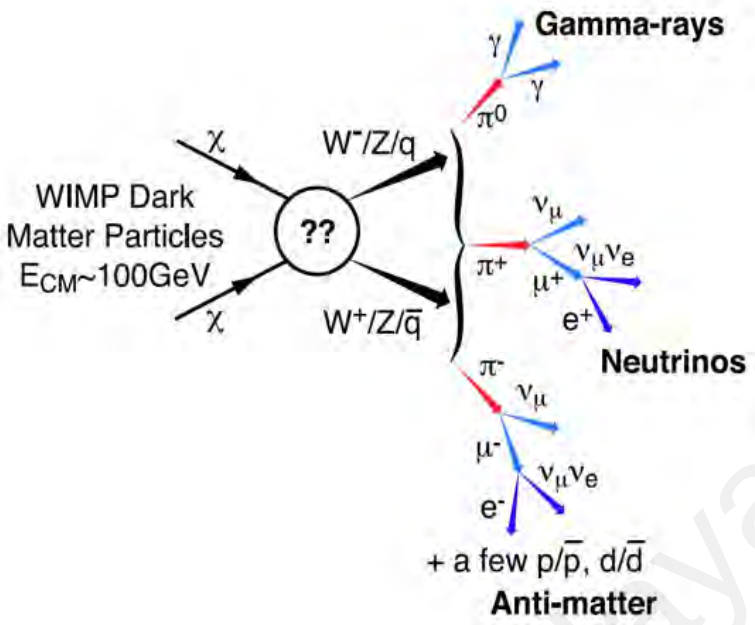

Figure 2.3: Pair annihilation of WIMPs (2 → 2 process) produces various SM particles (Image credit: Baltz et al., 2008).

Under the conservation of R-parity (a new quantum number in SUSY), the lightest supersymmetric particle does not decay. The neutral LSP is therefore a viable dark matter candidate. It is likely the neutralino (Goldberg, 1983; Ellis et al., 1984). There are, in fact, four neutralinos. They are all electrically neutral and colorless. The lightest of them is the dark matter candidate. The neutralino is a linear combination of the neutral higgsinos ($\tilde{H}_u^0$ and $\tilde{H}_d^0$) and neutral gauginos ($\tilde{B}$ and $\tilde{W}^0$). It is a Majorana particle (it is a fermion and it is its own antiparticle).

The self-annihilation of neutralinos can produce various SM particles. The heavy and unstable products will further decay into light and stable particles (e.g., protons, electrons, neutrinos, gamma ray, etc.). This study considered only the case where neutralinos annihilate into two-body final states (2 → 2 process).

2.3.2 Kaluza-Klein Dark Matter

The LKP is a particle from universal extra dimension (UED) theory. The extra dimension idea was first introduced by Klein (1926). It was later on developed into large

extra dimension (ADD) (Arkani-Hamed et al., 1999) and UED (Appelquist et al., 2001). In the theory of UED, all the SM particles can propagate into extra spacetime dimensions; while in ADD, only gravity propagates into the extra dimensions.

The simplest UED model where there is only one extra dimension was considered here. In the world of UED, all the SM particles that enter the extra dimension are accompanied by a tower of increasingly heavier states, called Kaluza-Klein (KK) states. A remnant of momentum conservation in the extra dimension is left in the form of conserved KK parity, which ensures that the lightest KK particle cannot decay and thus a viable dark matter. The LKP is likely to be the first KK excitation of the hypercharge gauge boson, denoted as $B^{(1)}$ (Cheng et al., 2002). It is a bosonic particle.

The annihilation of LKP can produce various SM particles in the same way as the LSP does, but it has a distinctive feature that it can annihilate into e^-e^+ pairs; while the Majorana nature of neutralino suppresses the light fermion channels as it requires one of the fermions to be helicity flipped.

2.4 Detections of Dark Matter

There are basically three types of search for dark matter particle, i.e., the direct and indirect detections, and the collider experiment. All the three searches are complementary to each other. Some of the searches are reviewed below, although none of the experiments claims a conclusive signal from the dark matter.

(a) ***Direct detection.***

The direct search is based on the interaction of dark matter with the ordinary matter. It looks for the nuclear recoil energy that results from the elastic scattering of dark matter particle off the known atomic nuclei in a low-background underground detector. The released results from XENON100 experiment (XENON100 Collaboration, 2013), which is

a dual-phase xenon time projection chamber in Italy, revealed no excess signal from WIMP interaction. The DarkSide-50, which searches for dark matter by using a two-phase liquid argon time projection chamber as detector, reported null result of search (Agnes et al., 2015). The reported data from PICO-2L experiment (PICO Collaboration, 2016), which utilizes a bubble chamber technique with C_3F_8 as active mass, showed no anomalous background events. The observed events from the LUX experiment (LUX Collaboration, 2016), a dual-phase xenon time projection chamber located in an underground laboratory in South Dakota, are consistent with the background-only model. All these non-detections were translated into limits on either the spin-dependent or spin-independent WIMP–nucleon scattering cross section.

(b) ***Indirect detection.***

In the indirect detection, one looks for the by-product radiation from the annihilation (or decay) of dark matter particles, such as the electrons, protons, neutrinos, and photons. The indirect search has an advantage that it can cover a wide range of photon frequency (from radio to gamma ray) due to the productions of photons by various secondary mechanisms, such as synchrotron emission, inverse Compton scattering, bremsstrahlung, and pion decay (Colafrancesco & Mele, 2001; Ackermann et al., 2010; Storm et al., 2013; Caputo et al., 2016). Since the dark matter particle annihilation rate is proportional to the dark matter particle number density, one always searches for the signal from the direction of dark-matter-rich source, e.g., the Galactic Center, dwarf galaxies, galaxy clusters, and even the Sun. An example of indirect detection is the search for an excess of neutrino flux above the atmospheric neutrino background in the Sun direction by Super-Kamiokande, which is a water Cherenkov neutrino detector. Super-Kamiokande Collaboration (2011) found no significant excess and derived an upper limit on the spin-dependent WIMP-nucleon scattering cross section. The IceCube, a neutrino telescope that uses a cubic kilometre

of glacial ice as detector medium, located in the South Pole, searches for the dark matter annihilation signal from the Milky Way. No excess was found in the search (IceCube Collaboration, 2016). Fornengo et al. (2014) analysed the cosmic-ray antiproton spectrum measured by PAMELA and found no deviation from the astrophysical background. Caputo et al. (2016) analysed a six years data of Fermi Large Area Telescope (LAT) to search for the dark-matter-induced-gamma-ray-signals from the Small Magellanic Cloud, which is a satellite galaxy of the Milky Way. Again, no excess signal from dark matter annihilation was found. Upper limits on the WIMP annihilation cross section were derived by these authors using the null searches.

(c) ***Collider experiment.***

The collider experiment collides two SM particles at high energy and aims to produce dark matter particles in the collisions. Several examples of such high energy colliders are the Tevatron (Bai et al., 2010), Large Electron Positron Collider (Fox et al., 2011), and Large Hadron Collider (LHC) (ATLAS Collaboration, 2016). In this type of search, the presence of dark matter particle is revealed as missing transverse momentum in the detection. Typically, one is looking for the events with one or two energetic jets and large missing transverse momentum in the final state. The search for such signature is often called the mono-jet search. Limits on dark matter–nucleon scattering cross section were placed by using the good consistency of the search result with the SM prediction (CMS Collaboration, 2015). A multijet search that instead looks for events with at least two jets (and missing transverse momentum) is also possible in LHC. A multijet search was performed by Buchmueller et al. (2015) using the data collected by CMS experiment. The dark matter model with pseudoscalar-mediated interaction was constrained in the search. Besides that, the LHC also searches for the decays of mediator, who is responsible for mediating the interaction between dark matter and SM particles, back into the SM particles.

The dark matter particle is not directly involved in this search. The null search for a dijet resonance was translated into limit on the properties of mediator and dark matter particle (CMS Collaboration, 2017). Another example of collider search is the search by Esmaili et al. (2017) who studied the photon-photon fusion process and translated the sensitivity of LHC to the process into constraint on the production of monochromatic gamma-ray in dark matter annihilation.

The collider search probes the interaction between dark matter and SM particles. However, even if it finds a 'dark' particle, this type of search is unable to prove that the particle is same as the one composes the main matter component in the universe. It is unable to probe the lifetime of the dark particle.

2.5 Hints for Dark Matter

(a) ***Dark matter annual modulation signature.***

Due to the Earth's revolution around the Sun, which is moving in the Milky Way, the Earth is expected to be crossed by a flux of dark matter particle that is maximum around 2 June and minimum around 2 December. The DAMA project is designed to find this dark matter annual modulation signature. The DAMA/LIBRA–phase1, together with the former DAMA/NaI experiment (both made of highly radiopure NaI(Tl) crystal scintillators), collected a total data of 1.33 ton $\times$ yr in 14 annual cycles. An annual modulation that satisfies all the dark matter interpretation is indeed observed at 9.3σ level (Bernabei et al., 2015).

(b) ***Cosmic ray anomalies.***

ATIC instrument detected a rise in the galactic cosmic ray electrons in excess over the conventional cosmic ray propagation model at energy ~300–800 GeV (Chang et al., 2008). An increase in cosmic ray positron fraction in 1.5–250 GeV is also confirmed by many

instruments such as PAMELA, AMS-02, and Fermi-LAT (Adriani et al., 2009; Aguilar et al., 2013; Ackermann et al., 2012). Possible explanations to these cosmic ray anomalies are the nearby pulsars (Profumo, 2012; Cholis & Hooper, 2013) and dark matter (Chang et al., 2008; Bhupal Dev et al., 2014).

(c) ***Gamma-ray excess from Galactic Center.***

The Galactic Center is expected to host a large concentration of dark matter. The evidence to an extended gamma-ray emission in the Milky Way's Galactic Center has been found by several analysis. The analysis is very challenging due to the lack of knowledge about the complicated background emission in the Galactic Center. Hooper and Goodenough (2011) found a component of gamma-ray emission at 1–4 GeV within the 1.25° inner radius of the Galactic Center. This excess emission is not consistent with any known astrophysical backgrounds, but it can be well explained by the annihilating dark matter interpretation. On the other hand, Boyarsky et al. (2011) argued that the gamma ray emission in the Galactic Center is actually consistent with the diffuse backgrounds and known point sources; there is no excess in the emission and therefore no additional ingredients are required. Abazajian et al. (2014) analyzed Fermi-LAT data, and found a robust detection of the extended Galactic Center emission at ∼1 GeV, whose morphology and spectrum are consistent with the dark matter annihilation and/or a population millisecond pulsars. Abramowski et al. (2015) analysed the data from H.E.S.S. telescope, which is a gamma-ray telescope that operates at very high energy domain, to search for the annihilation signal of dark matter, but no significant signal was found.

2.6 Diffuse Radio Emission

Human eyes respond only to a very narrow range of electromagnetic spectrum (the visible light). In astronomy, the observations in multi-wavelength are necessary in order to

have a complete picture of an astronomical object, as each wavelength shows some specific information about the object. For example, the hot gas in galaxy cluster can be studied in X-ray; the ultraviolet radiation is the signature from very hot stars; the infrared observation is essential in studying the cool stars and star forming regions; while radio emission tells the existence of relativistic electrons moving in the environment of magnetic field.

The radio wave is the electromagnetic wave with wavelength greater than 1 mm. In radio astronomy, there are two types of radio emission: (i) spectral line and (ii) continuum emissions. The line emission is the emission associated with the electron transition or any changes in quantum state. They are emitted at specific wavelengths and appear as "spikes" in the observed spectrum. The continuum emission, on the other hand, is the radiation that smoothly spreads over a wide range of frequencies. The continuum emission can be further classified into two: (i) thermal and (ii) non-thermal emissions. The thermal emission is determined by the object's temperature. The two sources of thermal emission are the blackbody radiation and thermal bremsstrahlung (free-free emission). Non-thermal emission refers to the emission that cannot be described by the blackbody and thermal bremsstrahlung, e.g., synchrotron emission and inverse-Compton radiation.

There are two radio emitting sources in the galaxy cluster: (i) the emission related to individual galaxies and (ii) the diffuse radio emission. The former is powered by the active galactic nucleus (AGN) and often shows radio jets and lobes; while the latter is non-thermal, of low surface brightness, and not associated with any cluster member. The diffuse radio emission shows steep radio spectral index, therefore it is best observed at low frequencies ($\leq$1.4 GHz). It is synchrotron in nature and reveals the presence of relativistic electrons and the cluster-wide magnetic field. Due to its low surface brightness, the discrete sources have to be subtracted before revealing the diffuse emission.

The diffuse radio emission can be categorized into three classes: radio haloes, radio mini-haloes, and radio relics. Figure 2.4(a), (b), and (c) show the three from different galaxy clusters. Radio halo is centrally located in the galaxy cluster and Mpc in scale. It spatially coincides with the X-ray morphology of galaxy cluster, and is regular in shape. Mini-halo is also centrally located in the galaxy cluster but much smaller than radio halo in physical size (≤500 kpc). It only appears at the center of a cool-core cluster, surrounds the radio-loud brightest cluster galaxy (BCG) but extends much beyond it. Radio relic is elongated in shape and located in the cluster periphery. It often exhibits strong polarization (20–30%) (Bonafede et al., 2009; van Weeren et al., 2010; de Gasperin et al., 2015).

2.6.1 Origin of diffuse radio emission

The origin of energy supplied to the relativistic electrons is still unclear. Relativistic electrons radiate their energy through synchrotron and inverse Compton emission. It implies that the electrons can only travel ∼100 kpc at most (assuming γ=300, diffusion velocity ∼ 100 km s^{-1}), which is far too small to cover the size of a radio halo. A significant re-acceleration or in situ energization is therefore necessary (Kuo et al., 2004). Currently there are two proposed origins of the relativistic electrons – (i) re-acceleration model (Brunetti et al., 2001; Petrosian, 2001) and (ii) secondary electron model (Dennison, 1980; Blasi & Colafrancesco, 1999).

(a) ***Re-acceleration model.***

In this model, the electrons were injected into the intracluster medium (ICM) during an "injection phase" in the past, through, e.g., starbust and AGN activities. These electrons lose energy over time, until a turbulence or shocks (induced by merger events) re-accelerate them into relativistic state again. This model predicts radio halo only in massive and merging system. As the turbulence stays only for a finite time, the radio halo is predicted

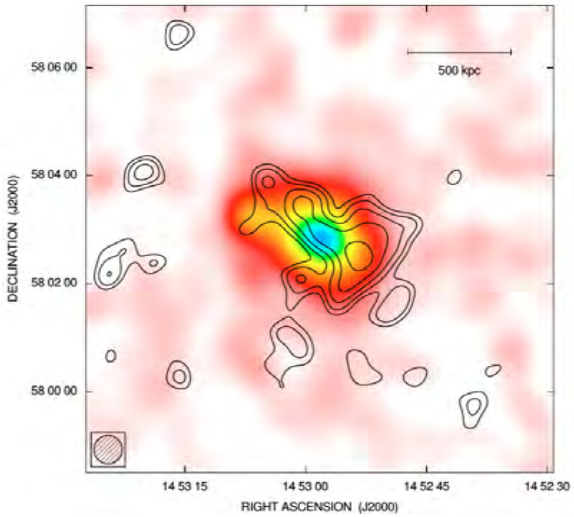

(a) Radio halo (contours) of A1995 at 1.4 GHz, overlaid on X-ray image in 0.1–2.4 keV band (Image credit: Giovannini et al., 2009).

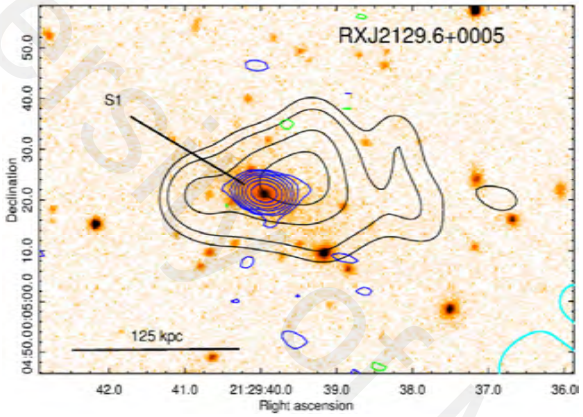

(b) Mini-halo in contours (black positive and cyan negative) of RXJ2129.6+0005 at 610 MHz, overlaid on the SDSS r-band image. S1 (the central compact source) is the BCG (Image credit: Kale et al., 2015).

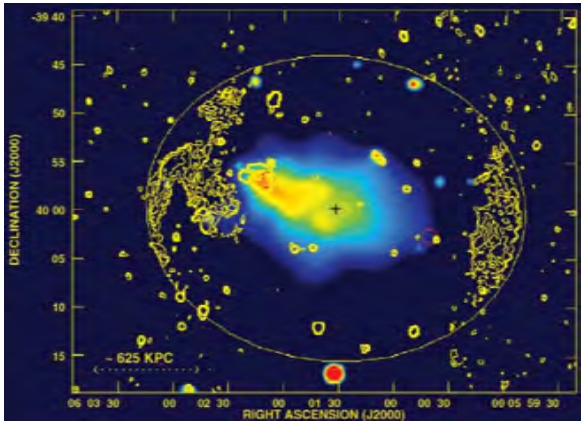

(c) Double radio relics (yellow contours) in A3376 at 1.4 GHz, overlaid on X-ray emission in 0.14–2.0 keV band (Image credit: Bagchi et al., 2006).

Figure 2.4: Radio halo, mini-halo, and radio relic.

to be a transient phenomenon and not common in galaxy clusters. In fact, observations show that radio halo is not ubiquitous in galaxy clusters. Currently they are seen only in ≈30% of massive galaxy clusters (Cassano et al., 2008; Venturi et al., 2008; Kale et al., 2015). The galaxy clusters have a bimodal distribution in $P_{1.4}$–L_X plane (Brunetti et al., 2007): clusters that host a radio halo follow a $P_{1.4}$–L_X correlation; whereas those without a radio halo have only the upper limits on radio halo lying one order of magnitude below the correlation. Besides that, Cassano et al. (2010) and Cuciti et al. (2015) confirmed that the radio halos are associated with dynamically disturbed clusters, supporting the re-acceleration model.

In the case of mini-haloes, the turbulence in re-acceleration model is not triggered by a merger event. In fact, the cool-core cluster, which is the host cluster of mini-halo, is usually a dynamically relaxed cluster. The core of a cool-core cluster exhibits a strong peak in the X-ray surface brightness and significant drop in temperature. It often hosts a BCG at the location of X-ray emission peak (Hudson et al., 2010). The energy loss due to X-ray emission is balanced by the feedback from the AGN of BCG. The turbulence in the case of mini-halo is associated with the cool-core region (Gitti et al., 2002). Mazzotta and Giacintucci (2008) observed that the mini-halo is confined within the cold front pairs, suggesting the sloshing of cluster core gas as the origin of turbulence.

For the radio relics, it is believed that they trace the shock fronts resulting from merger event (Enßlin et al., 1998). The X-ray observations on the radio relic (Solovyeva et al., 2008; Finoguenov et al., 2010) support this model. In this model, the ICM is compressed at the shock front, forcing the unordered magnetic field to align parallel to the shock front. The aligned magnetic field causes the radio emission to be highly polarized. This is supported by the detection of significant polarization in radio relic (van Weeren et al., 2010).

(b) ***Secondary electron model.***

The secondary electron model is based on the fact that the relativistic protons have negligible energy loss through radiation, due to its large mass, therefore they are expected to diffuse over ~1 Mpc; the inelastic collisions between these relativistic protons and thermal ions in ICM produce electrons as secondary products. This mechanism provides a continuous injection of relativistic electrons into the ICM. Numerical simulations by Dolag and Enßlin (2000) and Miniati et al. (2001) showed that this mechanism is able to produce the radio halos. The radio halo in this model is predicted to be a long-living phenomenon, therefore it should be common in galaxy clusters. However, it is disfavoured by the rare occurrence and bimodal distribution of galaxy clusters in $P_{1.4}$–L_X plane (Brunetti et al., 2007). Besides the inelastic collision between the protons and ambient gas, Colafrancesco and Mele (2001) suggested the neutralino annihilation as the origin of relativistic electrons and found that it is able to reproduce the radio halo of the Coma cluster. Marchegiani and Colafrancesco (2016) showed that the inclusion of observed distribution of dark matter sub-halos is able to reproduce the spectral and spatial properties of the radio halo in Coma cluster, without producing a gamma-ray flux in excess of the Fermi-LAT limits. However, the adopted dark matter particle models do not agree with the positron excess measured with AMS (Accardo et al., 2014). An interesting study by Brown and Rudnick (2011) found a puzzling correspondence between the brighter part of radio halo and the surface mass distribution derived from weak lensing, strengthening the dark matter as the origin of radio halo.

CHAPTER 3: METHODOLOGY

In order to set constraint on the dark matter particle properties, a comparison is to be made between the expected emission from the dark matter and observed diffuse radio emission. Several assumptions were used throughout this study: (i) The diffuse radio emission from a galaxy cluster was assumed to be solely from the dark matter annihilation. Although many current observations favour the re-acceleration mechanism as the origin of diffuse radio emission, the application of it to constrain the dark matter properties is robust; (ii) The dark matter was assumed to consist of only one type of particle, all dark matter particles have therefore exactly the same properties (charge, spin, mass, annihilation cross-section, annihilation channel, and etc.); (iii) The dark matter was assumed to be spherically distributed; (iv) A ΛCDM was used throughout this study, with Hubble constant $H_0 = 100\ h$ km s^{-1} Mpc^{-1}, Hubble parameter $h = 0.7$, $\Omega_m = 0.3$, and $\Omega_\Lambda = 0.7$. The subscripts m and Λ here denote the matter and dark energy components, respectively; (v) The baryonic content is negligible, the dark matter therefore contributes 100 % to the massive matter.

The steps that were taken to conduct this study are summarized in Figure 3.1. This chapter describes in details the procedures to estimate the expected synchrotron flux density due to dark matter annihilation.

3.1 Sample Selection

The sample consisted of six galaxy clusters with z lower than one. All these clusters had previously been observed and analysed in radio frequency, using the data from different radio telescopes: the Coma cluster is known to host a giant radio halo at the centre (Venturi et al., 1990); galaxy clusters 2A0335 and A478 host mini-haloes (Giacintucci et al., 2014); while no diffuse radio emission is found in three galaxy clusters (i.e., A1367, A2199 and

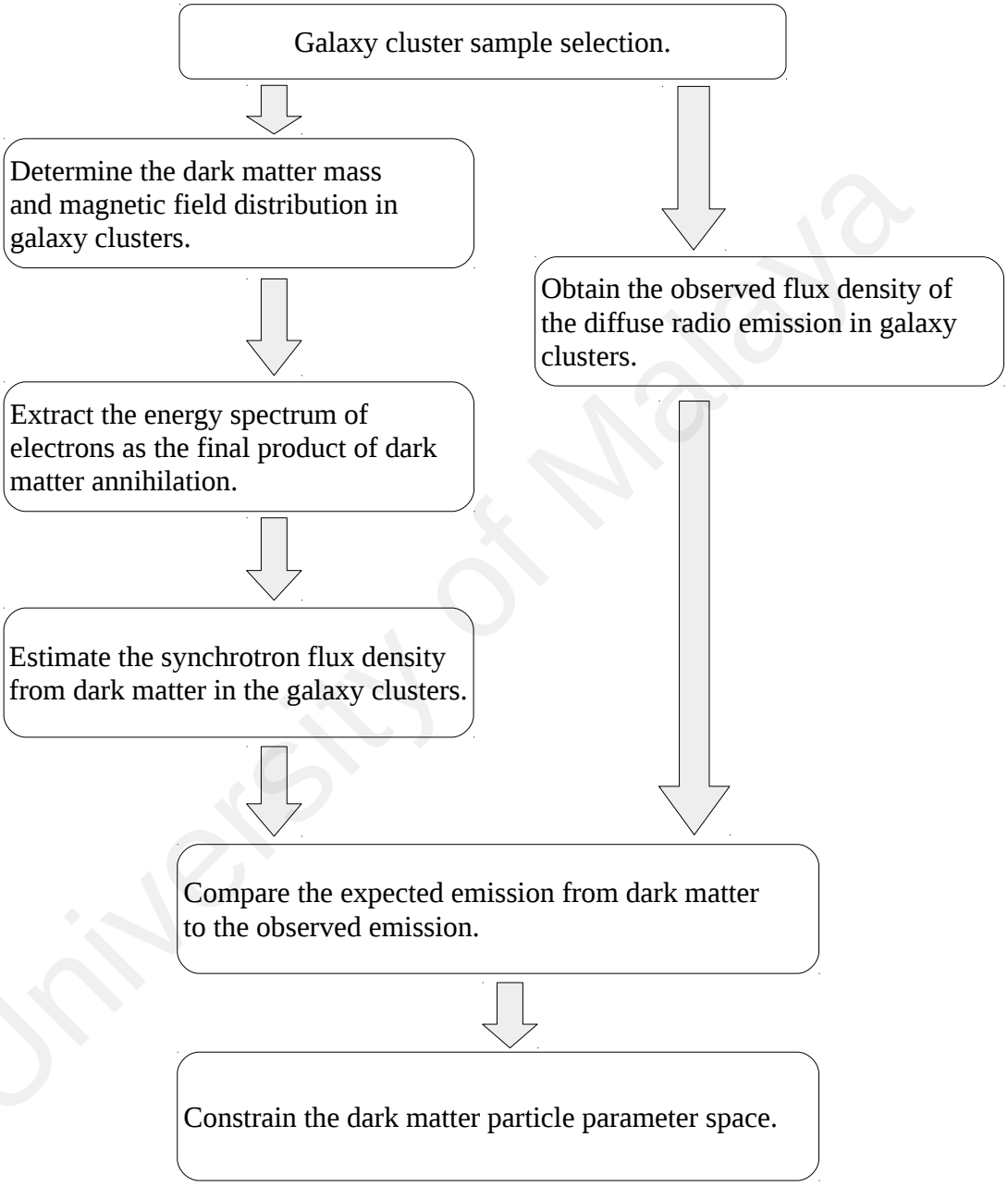

Figure 3.1: Procedures to constrain the dark matter particle properties.

A119), but the upper limits on their radio halo detections have been placed (Farnsworth et al., 2013; Rudnick & Lemmerman, 2009). Note that a galaxy cluster without any diffuse radio emission detected is in fact the best target to constrain the dark matter particle properties. Here the clusters with diffuse radio emission detected were included as well for comparison purpose. The type of emission, observation frequency, size, and flux density of emission are listed in Table 3.1.

3.2 Dark Matter Density Distribution in Galaxy Clusters

The distribution of dark matter in a celestial object is often expressed as the halo density profile. The structure of dark matter halo has been studied by several authors before using the high resolution N-body simulations (Navarro et al., 1997; Moore et al., 1999; Navarro et al., 2004; Diemand et al., 2005) and empirically (Burkert, 1995; Kravtsov et al., 1998). Different studies suggest different density profiles, especially at the innermost region of halo. In general, the dark matter halo profile can be described by an $\alpha\beta\gamma$-profile, which has the following form:

$$\rho(r) = \frac{\rho_s}{(r/r_s)^{\gamma}[1 + (r/r_s)^{\alpha}]^{(\beta-\gamma)/\alpha}}, \tag{3.1}$$

where (α, β, γ) defines the profile shape as suggested by different studies, and (ρ_s, r_s) reflects the properties of individual halo. The profile with shape other than the general $\alpha\beta\gamma$-profile is possible as well (Navarro et al., 2004; Burkert, 1995). Figure 3.2 shows the inner region of a halo described by different profile models. Due to the limitation of the simulation resolution, there is still no agreement on the profile shape at the inner region.

In this study, the smooth density profile suggested by Navarro et al. (1997) (hereafter NFW) was adopted to represent the gravitational mass distribution of galaxy clusters. The NFW profile has $(\alpha, \beta, \gamma) = (1, 3, 1)$, which is cuspy at the central region. The divergent

Table 3.1: Diffuse radio emissions from galaxy clusters.

Name	Type	ν	S_ν	R	Telescope	Reference
	-	(GHz)	(mJy)	(kpc)	-	-
A1367	upper limit on radio halo	1.4	<148	<500	GBT–NVSS	(Farnsworth et al., 2013)
Coma	radio halo	0.326	3810	586.94[a]	WSRT	(Venturi et al., 1990)
A2199	upper limit on radio halo	0.327	<250	<500	WENSS	(Rudnick & Lemmerman, 2009)
2A0335	mini halo	1.4	21.1	70	VLA	(Giacintucci et al., 2014)
A119	upper limit on radio halo	1.4	243	533.7[b]	GBT–NVSS	(Farnsworth et al., 2013)
A478	mini halo	1.4	16.6	160	VLA	(Giacintucci et al., 2014)

[a] Average of the extension of radio halo, taken as $R = 0.5 \times \sqrt{44' \times 40'}$.

[b] Average of the observed major and minor angular dimensions, taken as $R = 0.5 \times \sqrt{27.2' \times 15.5'}$.

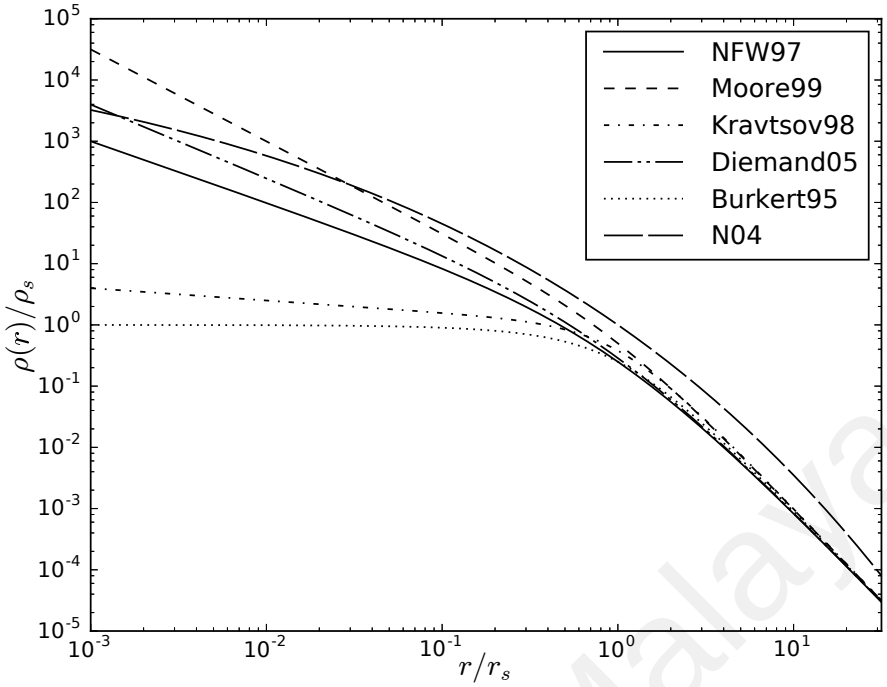

Figure 3.2: Density profiles of a halo in the inner region as described by different profile models.

property of the NFW profile at the center does not pose a problem in this work as the region interested in this study is far larger than the scale in which the error can be seen. It is therefore fair enough to assume an NFW distribution. Navarro et al. (1997) suggested that dark haloes are universal in shape, in the sense that the shape of profile has no dependence on the cluster mass.

Besides (ρ_s, r_s), the NFW profile is often characterized in terms of virial concentration (c_{vir}) and virial mass (M_{vir}). The virial mass of a halo is defined as the total mass enclosed in the radius (which is virial radius r_{vir}) within which the average density is an overdensity (Δ_c) above the critical density of the universe:

$$\begin{aligned} M_{vir} &= \frac{4}{3}\pi\Delta_c\rho_{crit}r_{vir}^3 \\ &= \frac{4}{3}\pi\Delta_{vir}\rho_m r_{vir}^3 \end{aligned} \tag{3.2}$$

where $\rho_m = \Omega_m \rho_{crit}$, $\rho_{crit} = \frac{3H^2}{8\pi G}$, and $\Delta_c = \Delta_{vir}\Omega_m$. The objects within r_{vir} are virialized – they are bounded by gravitational force, pressure-supported and slightly rotating. Bryan and Norman (1998) provided the expression for the overdensity of a virialized halo:

$$\Delta_c = 18\pi^2 + 82x - 39x^2, \tag{3.3}$$

where $x = \Omega_m(z) - 1$ and

$$\Omega_m(z) = \frac{1}{1 + (\Omega_{\Lambda,0}/\Omega_{m,0})(1+z)^{-3}}. \tag{3.4}$$

The subscript "0" here indicates the value at present day.

For an NFW profile, the virial concentration is defined as $c_{vir} = r_{vir}/r_s$. It indicates the compactness of a halo. The total mass enclosed within a radius r in an NFW profile can be obtained by doing volume integration on the NFW density profile:

$$\begin{aligned} M(<r) &= 4\pi \int_0^r r^2 \rho(r)\, dr \\ &= 4\pi \rho_s r_s^3 \left[\ln(1 + r/r_s) - \frac{r/r_s}{1 + r/r_s} \right]. \end{aligned} \tag{3.5}$$

By equating Equation (3.2) and Equation (3.5) at $r = r_{vir}$, the value of ρ_s is determined by

$$\frac{\rho_s}{\rho_{crit}} = \frac{\Delta_c}{3} \frac{c_{vir}^3}{\ln(1 + c_{vir}) - c_{vir}/(1 + c_{vir})}. \tag{3.6}$$

Many studies have been conducted to find a correlation between c_{vir} and M_{vir}, through simulations (Bullock et al., 2001; Prada et al., 2012) and observations (Buote et al., 2007; Comerford & Natarajan, 2007). Different studies yield a different power-law index in the c_{vir}–M_{vir} correlation. Groener et al. (2016) collected a large sample of galaxy clusters

whose mass have been reconstructed using different techniques (i.e., weak and strong lensing, X-ray, line-of-sight velocity dispersion (LOSVD), and caustic method (CM)) to study the observational c_{vir}–M_{vir} relation. This study made use of Table A1 from (Groener et al., 2016) to derive the NFW density profile of sample galaxy clusters. The cluster properties (c_{vir} and M_{vir}) are listed in Table 3.2, where the $M_\odot$ represents the mass of the Sun. Figure 3.3 shows their density profiles.

Table 3.2: NFW profile parameters of galaxy clusters.

Name	z	c_{vir}	M_{vir}	Method	Reference
	-	-	10^{14} $M_\odot$	-	-
A1367	0.0216	21.9	6.11	CM	(Rines et al., 2003)
Coma	0.0231	13.1	12.9	CM	(Rines et al., 2003)
A2199	0.0302	10.4	7.1	LOSVD	(Łokas et al., 2006)
2A0335	0.0349	10.7	1.6	X-ray	(Voigt & Fabian, 2006)
A119	0.0440	5.59	30.2	X-ray	(Babyk et al., 2014)
A478	0.0880	6.01	28.72	X-ray	(Babyk et al., 2014)

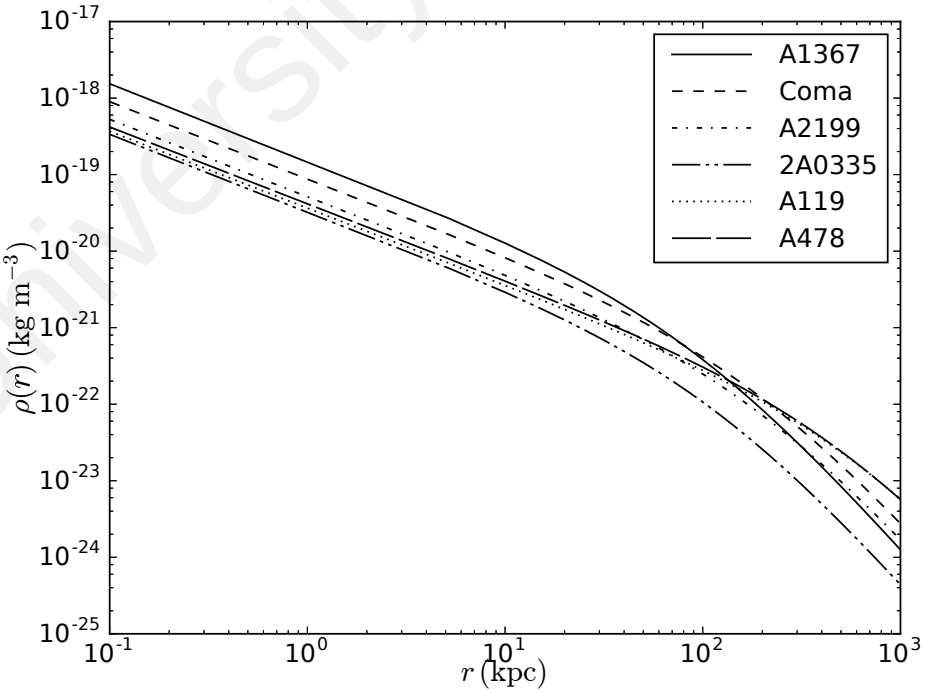

Figure 3.3: Adopted NFW density profiles of the galaxy clusters. Profiles are determined by using the M_{vir} and c_{vir} values from Table A1 of (Groener et al., 2016).

By assuming the dark matter to compose of one type of dark matter particle (χ) only, the dark matter particle number density is

$$N_\chi(r) = \frac{\rho_{DM}(r)}{m_\chi}, \tag{3.7}$$

where $\rho_{DM}(r)$ is given in Equation (3.1), and m_χ is the dark matter particle mass. Note that the gas component is not subtracted in the estimation of dark matter mass, since the gas fraction is only (0.10 ± 0.05) of the total mass in the galaxy clusters (Allen et al., 2004).

3.3 Cluster Magnetic Field

The ICM is found to permeate with magnetic field of order 1 μG (see Carilli & Taylor, 2002; Feretti et al., 2012, for reviews). The presence of cluster magnetic field can be revealed from the diffuse radio emission (radio haloes, mini-haloes, and radio relics), thanks to its synchrotron nature. One of the widely used techniques to measure the cluster magnetic field is the Faraday rotation measure, which is based on the principle that the polarization angle of the radiation from a polarized radio galaxy rotates as the radiation travels through a magnetized plasma.

The intracluster magnetic field is far from being a uniform field, it declines with cluster radius. The profile of cluster magnetic field strength shows a good scaling relation with the intracluster gas density distribution (n_{gas}) (Dolag et al., 2001):

$$\begin{aligned} B(r) &\propto n_{gas}(r)^\eta \\ &= B_0\Big(1 + \frac{r^2}{{r_c}^2}\Big)^{-(3/2)\beta\eta} \end{aligned} \tag{3.8}$$

where B_0 and η are the central magnetic field and proportional index, respectively; while r_c is the core radius and β is the parameter in the standard β-model, which describe the

cluster gas density profile. A lower η denotes that the cluster magnetic field decreases less rapidly with increasing distance from the cluster center. Equation (3.8) was adopted as the cluster magnetic field profile in this study.

Among the six galaxy clusters in the sample, three (i.e., the Coma cluster, A2199, and A119) have previously been studied about their intracluster magnetic field (Bonafede et al., 2010; Vacca et al., 2012; Dolag et al., 2001), by using Faraday rotation measure. The values of their B_0 and η used in the work were taken from the respective literatures.

A1367, 2A0335, and A478 have no report on their magnetic field properties. Clusters 2A0335 and A478 are cool-core clusters, whereas A1367 shows no evidence of a cool-core (Chen et al., 2007; Eckert et al., 2011). The cool-core cluster tends to have a much higher central magnetic field ($10 - 40$ μG) as compared to the non-cool-core cluster (Carilli & Taylor, 2002; Kuchar & Enßlin, 2011; Taylor et al., 2002). For the cool-core clusters (2A0335 and A478), their central magnetic fields were assumed to be 10 μG in this work; while 1 μG was assumed for the non-cool-core cluster (A1367). The study on magnetic field shows that the value of η lies between 0.5 and 1.0 (Dolag et al., 2001). For these three galaxy clusters that have no report on η values, their η were taken to be 1.0. By taking the upper bound on η, a steeper declined magnetic field is assumed, which would be expected to translate to a lower bound on synchrotron flux (equivalent to an upper bound on the $\langle\sigma v\rangle$–m_χ upper limit constraint).

The properties of the magnetic field of the sample galaxy clusters are listed in Table 3.3. The last column, $n_{gas,0}$, shows the central gas density of the galaxy cluster. The magnetic field profiles of the sample are plotted in Figure 3.4.

Table 3.3: Magnetic field properties of galaxy clusters.

Name	β -	r_{core} (kpc)	B_0 (μG)	η -	Cool-core -	$n_{gas,0}$ (10^{-2} cm^{-3})
A1367	0.695	273.6	1.0*	1.0*	No	0.15[a]
Coma	0.654	245.0	4.7[b]	0.5[b]	No	0.342[c]
A2199	0.655	99.3	11.7[d]	0.9[d]	Yes	10.1[d]
2A0335	0.575	23.6	10.0*	1.0*	Yes	5.47[a]
A119	0.675	357.9	7.5[e]	0.9[e]	No	0.15[a]
A478	0.613	70.0	10.0*	1.0*	Yes	3.55[a]

*Assumed.
[a]Chen et al. (2007), [b]Bonafede et al. (2010), [c]Briel et al. (1992), [d]Vacca et al. (2012), [e]Dolag et al. (2001).

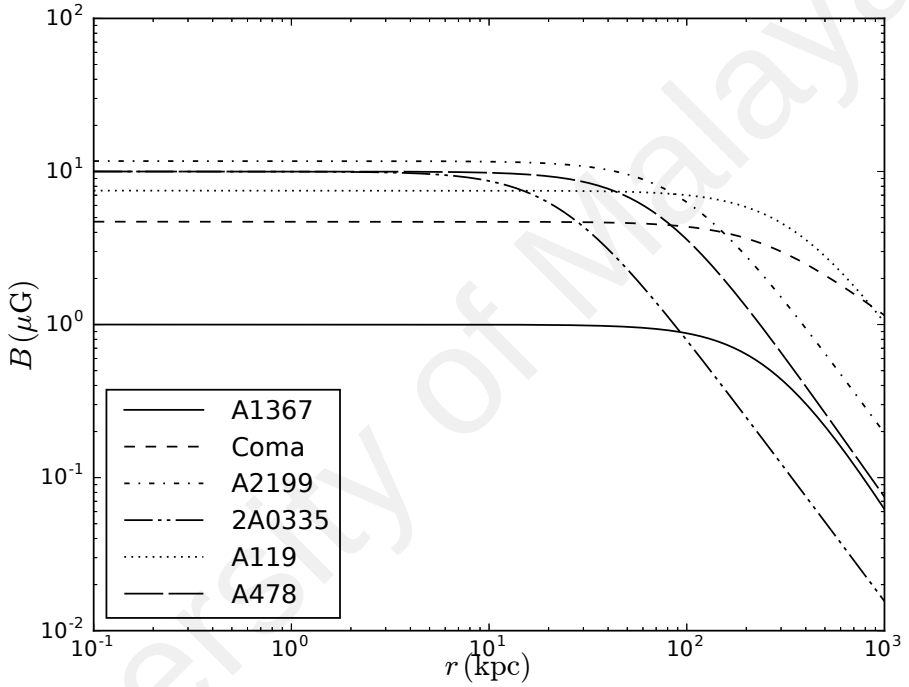

Figure 3.4: Adopted profiles of intracluster magnetic fields in the galaxy clusters.

3.4 Energy Spectrum of the Final State Products

The dark matter annihilation leads to different types of SM particles. The heavy and unstable annihilation products undergo decay chain and can eventually produce electrons and positrons (hereafter electrons) as one of the final products.

The electron energy spectrum $\frac{dN}{dE}$ tells the number and energies of final state electrons from the dark matter annihilation. It is dependent on the dark matter particle mass and the annihilation channel. The DARKSUSY package (Gondolo et al., 2015) was employed in

this study to obtain the energy spectra of the final electrons through different neutralino annihilation channel. DARKSUSY is a set of Fortran routine to make calculations for the Supersymmetric dark matter (neutralino in this study). It is capable to evaluate the annihilation products from different Supersymmetric scenarios, i.e., MSSM and mSUGRA. In fact, DARKSUSY does not simulate the hadronization and decay of the neutralino annihilation products, that has been simulated with the Monte Carlo code, PYTHIA, instead. The results from the PYTHIA are tabulated and used in DARKSUSY.

In the DARKSUSY, eight fundamental annihilation channels (Z^0Z^0, W^+W^-, $\mu^+\mu^-$, $\tau^+\tau^-$, $c\bar{c}$, $t\bar{t}$, $b\bar{b}$, gg) and six complex channels (H^0A^0, h^0A^0, Z^0H^0, Z^0h^0, W^+H^-/W^-H^+, $Z^0\gamma$) are included. All the particles in the fundamental channels are particles with known masses. Figure 3.5 shows the electron spectra from the fundamental channels with $m_\chi = 1000$ GeV. The $b\bar{b}$ and $\mu^+\mu^-$ channels are the two extreme channels among the fundamental channels. Any combination of the fundamental annihilation channels can be interpolated between the two extrema. Note that the $t\bar{t}$ channel produces a harder spectrum than $b\bar{b}$ channel does, however it is not always kinematically allowed due to its large mass. On the other hand, the electron spectra from the complex channels are dependent on the Supersymmetric scenario.

3.5 Expected Synchrotron Emission

This study adopts the model by Sarazin (1999) for the evolution of electron population in a galaxy cluster and the calculation of synchrotron radio emission. The evolution of electron population starts from the electron source spectrum $Q_e(r, E)$, which represents the rate of production of electrons (due to dark matter particle pair annihilation) per unit

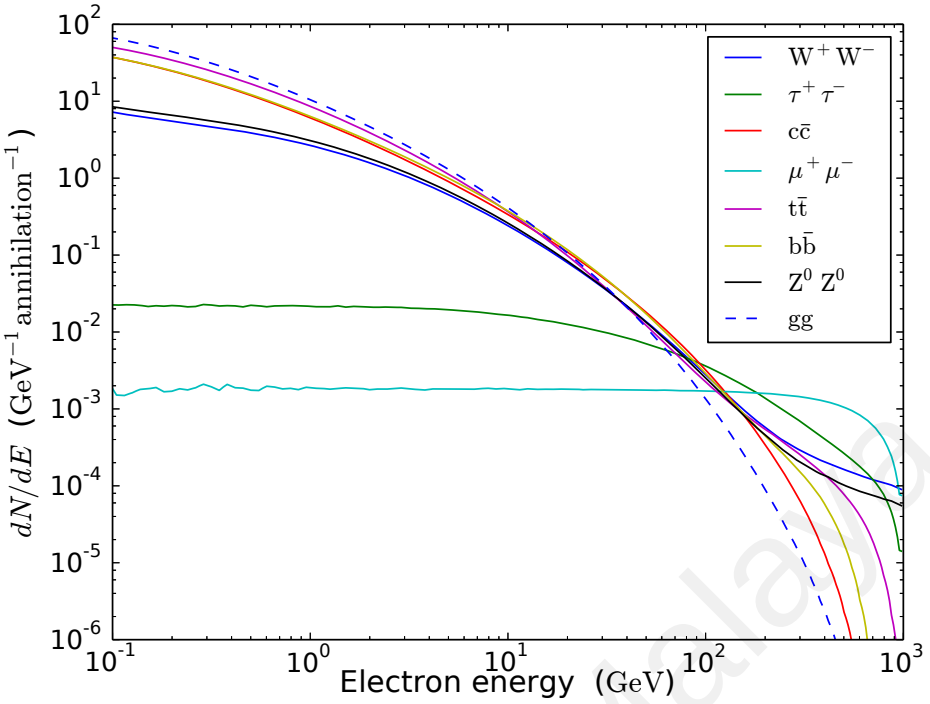

Figure 3.5: Yield of electrons per unit energy per neutralino annihilation through fundamental channels, for m_χ = 1000 GeV neutralino.

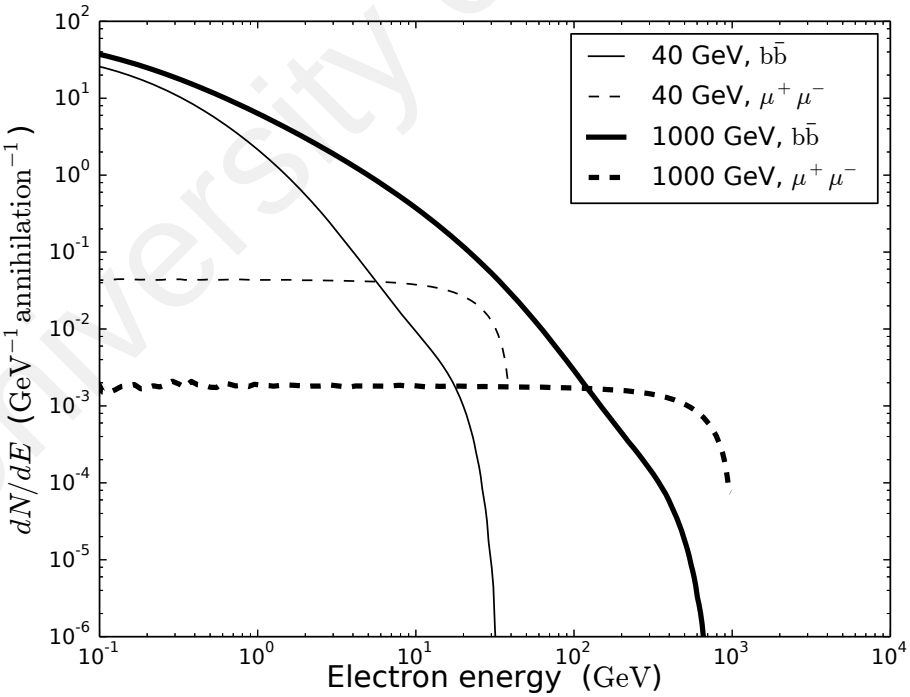

Figure 3.6: Yield of electrons per unit energy per neutralino annihilation, for m_χ = 40 GeV (thin) and m_χ = 1000 GeV (thick). Solid line shows BR($b\bar{b}$)=1; while dashed line shows BR($\mu^+\mu^-$)=1.

volume per unit energy. It is obtained by:

$$Q_e(r, E) = \sum_f \langle \sigma v \rangle \frac{dN^f}{dE} BR_f \frac{N_\chi(r)^2}{2}, \tag{3.9}$$

where f denotes the annihilation channel, BR the branching ratio into f channel, and $N_\chi(r)$ the dark matter particle number density as given in Equation (3.7). Note that the positron contributes equally to the synchrotron radiation. The source spectra in the following calculations were multiplied by a factor of two to take into account the contribution from positrons.

The charged final products are accelerated by magnetic fields in galaxy clusters. The magnetic fields in the galaxy clusters are not uniformly distributed but tangled; therefore, the evolution of electrons in the galaxy cluster is expressed by the diffusion-loss equation

$$\frac{\partial n_{eq}(r, E, t)}{\partial t} = \frac{\partial}{\partial E}[b(r, E)\, n_{eq}(r, E)] + Q_e(r, E), \tag{3.10}$$

where $n_{eq}(r, E, t)$ is called the electron equilibrium spectrum and $b(r, E)$ is the energy loss due to synchrotron emission, inverse Compton scattering, Coulomb radiation and bremsstrahlung radiation. Equation (3.11.1–3.11.4) show the expressions of each energy

loss term:

$$b_{syn}(E,B) = \frac{4}{3}\sigma_T c\beta^2 U_B\Big(\frac{E}{m_e c^2}+1\Big)^2$$
$$= 2.53\times10^{-18}\,\Big(\frac{E}{1\,\mathrm{GeV}}\Big)^2\Big(\frac{B}{1\,\mu\mathrm{G}}\Big)^2 \tag{3.11.1}$$
$$b_{IC}(E) = \frac{4}{3}\sigma_T c\beta^2 U_{CMB}\Big(\frac{E}{m_e c^2}+1\Big)^2$$
$$= 3.07\times10^{-17}\,(1+z)^4\,\Big(\frac{E}{1\,\mathrm{GeV}}\Big)^2 \tag{3.11.2}$$
$$b_{Coul}(E) = 6.13\times10^{-16}\,n_{gas}(r)\times\Big[1.0+\frac{\ln(\gamma/n_{gas}(r))}{75}\Big] \tag{3.11.3}$$
$$b_{brem}(E) = 7.72\times10^{-20}\,n_{gas}\,\gamma\times[\ln(\gamma)+0.36], \tag{3.11.4}$$

where n_{gas} is in unit of cm^{-3}, and all the four b_{loss} are in unit of GeV s^{-1}. γ is the Lorentz factor.

The dark matter annihilations continuously inject the electrons into the galaxy cluster. Eventually, the source electrons reach a time-independent equilibrium state. Taking the left-hand side of Equation (3.10) to be zero (so that n_{eq} is time-independent), it becomes:

$$n_{eq}(r,E) = \frac{1}{b(r,E)}\int_E^\infty Q_e(r,E')\,dE'. \tag{3.12}$$

The synchrotron radiation emissivity (ϵ_ν) of the relativistic electrons per unit volume with kinetic energy from E to $E+dE$, averaging over all pitch angles, is

$$\epsilon_\nu(r) = \frac{\sqrt{3}e^3}{m_e c^2}\int_E n_{eq}(r,E)\,R(x)\,B(r)\,dE, \tag{3.13}$$

where $R(x)$ is defined as (Ghisellini et al., 1988)

$$R(x) \equiv 2x^2\Big\{K_{4/3}(x)K_{1/3}(x) - \frac{3}{5}x\Big[{K_{4/3}}^2(x){K_{1/3}}^2(x)\Big]\Big\}, \tag{3.14}$$

where K is the modified Bessel function and $x = (2\pi {m_e}^3 c^5 \nu)/(3eBE^2)$. The symbols e, m_e, c and ν represent the elementary charge, electron mass, speed of light and photon frequency, respectively.

The total radio luminosity is computed by integrating $\epsilon_\nu(r)$ over the cluster volume. And then, the synchrotron radio flux density (S_ν) can be obtained by

$$S_\nu = \frac{4\pi \int_0^R r^2 \, \epsilon_\nu(r) \, dr}{4\pi D_L^2}, \tag{3.15}$$

where D_L is the luminosity distance of the galaxy cluster.

3.6 MSSM and mSUGRA Scenarios

There are many SUSY models, e.g., phenomenological MSSM, mSUGRA, the minimal gauge-mediated supersymmetry breaking model, natural gauge mediation, and etc., each having its own SUSY breaking mechanism and assumptions. The details about the two SUSY models in DARKSUSY (i.e., a phenomenological MSSM and mSUGRA models) can be found in (Gondolo et al., 2004).

In the phenomenological MSSM (and mSUGRA) scenario, the values of m_χ, BRs, and $\langle \sigma v \rangle$ are determined by the choice of MSSM (and mSUGRA) free parameters. The phenomenological MSSM model in DARKSUSY is characterized by seven parameters, which are the Higgsino mass parameter μ, gaugino mass parameter M_2, ratio of the two-Higgs-doublet vacuum expectation value (VEV) tan β, mass of CP-odd Higgs m_A, the common sfermion mass m_0, and the trilinear Higgs sfermion couplings to bottom and top squarks (A_b and A_t). Parameter space scanning on MSSM was performed using DARKSUSY. The synchrotron radio flux was then derived for each combination of MSSM parameters. For simplicity, A_t was set to be A_b. Only 20247 out of 84035 scanning sets obtained were not rejected by various accelerator constraints such as the lower bound on particle mass

and BR($b \to s\gamma$). The parameter values of the allowed sets are listed in Table 3.4. Note that not all combinations of the allowed parameters were acceptable for the results of the accelerator search.

Table 3.4: DARKSUSY MSSM parameters scanning values.

μ (GeV)	:	350, 650, 950, 1250, 1550, 1850
M_2 (GeV)	:	350, 650, 950, 1250, 1550, 1850
tan β	:	1, 21, 41, 61, 81
m_A (GeV)	:	50, 350, 650, 950, 1250, 1550, 1850
m_0 (GeV)	:	350, 650, 950, 1250, 1550, 1850
A_b/m_0	:	$\pm 3, \pm 2, \pm 1, 0$
A_t/m_0	:	$= A_b/m_0$

The scanning on parameter space was also performed on mSUGRA. The mSUGRA model relies on five free parameters, which are the common scalar and gaugino soft breaking masses at the grand unification scale (m_0 and $m_{1/2}$), the universal supersymmetry breaking trilinear scalar interaction A_0, the ratio of the two-Higgs-doublet VEV tan β and the sign of higgsino mass parameter μ. In total, 5353 combinations of mSUGRA parameters were obtained. The parameter values of the allowed sets are shown in Table 3.5.

Table 3.5: DARKSUSY mSUGRA parameters scanning values.

m_0 (GeV)	:	50, 800, 1550, 2300, 3050, 3800, 4550, 5300, 6050
$m_{1/2}$ (GeV)	:	50, 350, 650, 950, 1250, 1550, 1850, 2150
A_0 (GeV)	:	$\pm 4000, \pm 3000, \pm 2000, \pm 1000, 0$
tan β	:	5, 15, 25, 35, 45, 55, 65
sign(μ)	:	-1, +1

3.7 Kaluza-Klein Dark Matter

In the case of KK dark matter, the LKP is expressed as $B^{(1)}$ (see Section 2.3.2). The branching ratio of $B^{(1)}B^{(1)}$ annihilation was adopted from Table 2 of (Hooper & Profumo, 2007) and re-listed here in Table 3.6. The electron spectrum from $B^{(1)}B^{(1)}$ annihilation could then be computed using PYTHIA. This was performed for 400 GeV $\leq$ $m_{B^{(1)}} \leq$ 1200 GeV in this study.

Table 3.6: Branching ratio of $B^{(1)}B^{(1)}$ annihilation into various final states.

Process		BR
$B^{(1)}B^{(1)}$	$\rightarrow \nu_e\bar{\nu}_e, \nu_\mu\bar{\nu}_\mu, \nu_\tau\bar{\nu}_\tau$	0.014
	$\rightarrow e^+e^-, \mu^+\mu^-, \tau^+\tau^-$	0.23
	$\rightarrow u\bar{u}, c\bar{c}, t\bar{t}$	0.077
	$\rightarrow d\bar{d}, s\bar{s}, b\bar{b}$	0.005
	$\rightarrow \phi\phi^*$	0.027

Figure 3.7 shows the electron spectrum from a $B^{(1)}B^{(1)}$ annihilation event with $m_{B^{(1)}} = 800$ GeV. The electron spectra from neutralino annihilations ($b\bar{b}$ and $\mu^+\mu^-$) are plotted in the same figure for comparison. The spectrum from $B^{(1)}B^{(1)}$ annihilation falls between the two extreme neutralino spectra, except at the energy around $m_{B^{(1)}}$ where $B^{(1)}B^{(1)}$ annihilation shows a sharp edge. This sharp edge comes from the e^+e^- annihilation channel which is suppressed in the case of neutralino.

The synchrotron flux density was estimated in the same way as for the neutralino dark matter.

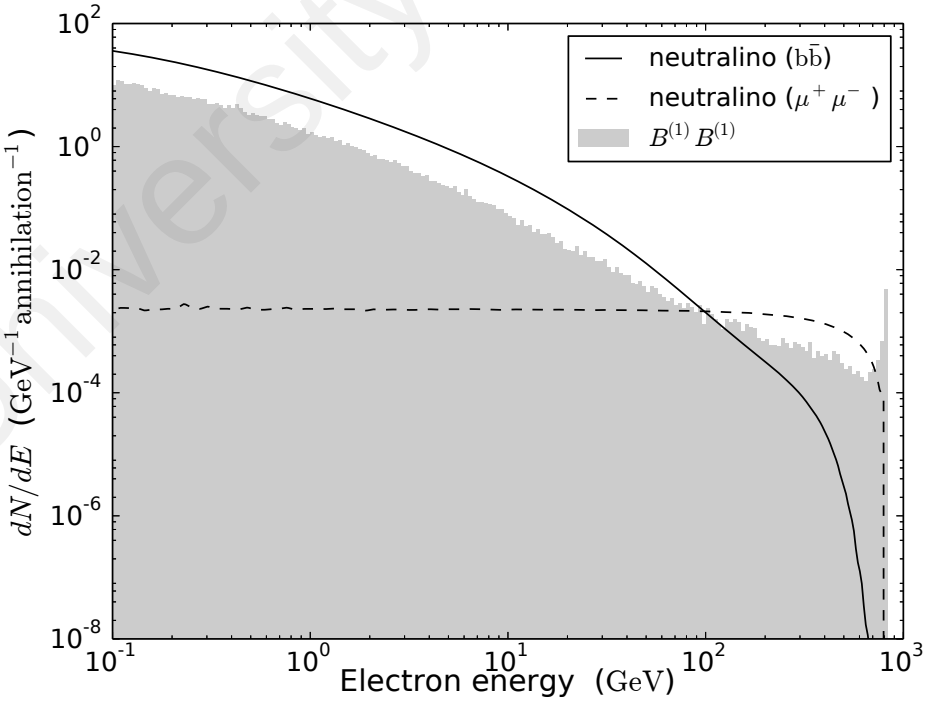

Figure 3.7: Number of final state electrons (not including positrons) per unit energy per $B^{(1)}B^{(1)}$ annihilation (grey shade). Neutralino annihilations through $b\bar{b}$ (solid line) and $\mu^+\mu^-$ (dashed line) channels are plotted for comparison. All plots assume 800 GeV dark matter particle mass.

CHAPTER 4: RESULTS AND DISCUSSIONS

4.1 Constraints on neutralino parameter space

The particle-physics-dependent term in the calculation of dark-matter-induced S_ν (Equation 3.9) is a function of $\langle\sigma v\rangle$ and $\frac{dN}{dE}$, the latter of which is dependent on the choice of annihilation channel and dark matter particle mass. This section considered only the neutralino annihilation through the extreme fundamental channels, i.e., $b\bar{b}$ and $\mu^+\mu^-$ channels. Twenty-six values of m_χ were selected from the range [40 GeV, 4000 GeV]. The electron energy spectrum per annihilation $\frac{dN}{dE}$ was extracted for each combination of annihilation channel and m_χ by using the DARKSUSY package. Fifteen values of $\langle\sigma v\rangle$ were chosen from $\log[\langle\sigma v\rangle/(1\ \mathrm{cm}^3\ \mathrm{s}^{-1})] = [-31, -22]$. In total, $26 \times 15 = 390$ combinations of m_χ and $\langle\sigma v\rangle$ were produced for each annihilation channel.

The electron source spectrum $Q_e(r, E)$ (and therefore the expected annihilation signal S_ν) could then be derived according to the steps described in Section 3.5. With the expected S_ν derived from different combinations of m_χ, $\langle\sigma v\rangle$, and annihilation channel, the next step was to write out the explicit relation between the expected S_ν, m_χ, and $\langle\sigma v\rangle$. This was achieved by performing a non-linear least squares fitting on the expected $S_\nu/\langle\sigma v\rangle$ versus m_χ data, which is shown in Figure 4.1. This explicit relation was required so that the observed radio flux density could later on be substituted into the relation to derive the upper limit constraint on $\langle\sigma v\rangle$–m_χ space. The data points in Figure 4.1 could generally be described by a function in the form of

$$\log_{10}\left(\frac{S_\nu}{\langle\sigma v\rangle}\right) = c_1 \log_{10}(m_\chi + c_2) + c_3, \tag{4.1}$$

which would lead to a constraint as below:

$$\langle \sigma v \rangle \leq 10^{\log_{10} S_\nu - c_1 \log_{10}(m_\chi + c_2) - c_3}, \tag{4.2}$$

where c_1, c_2 and c_3 are the constants from curve fitting. S_ν, $\langle \sigma v \rangle$ and m_χ are in units of mJy, $\mathrm{cm}^3\,\mathrm{s}^{-1}$ and GeV, respectively. The curve fitting was made for each annihilation channel and shown as lines in Figure 4.1 (only A1367). The values of the fitting constants for all galaxy clusters are listed in Table 4.1.

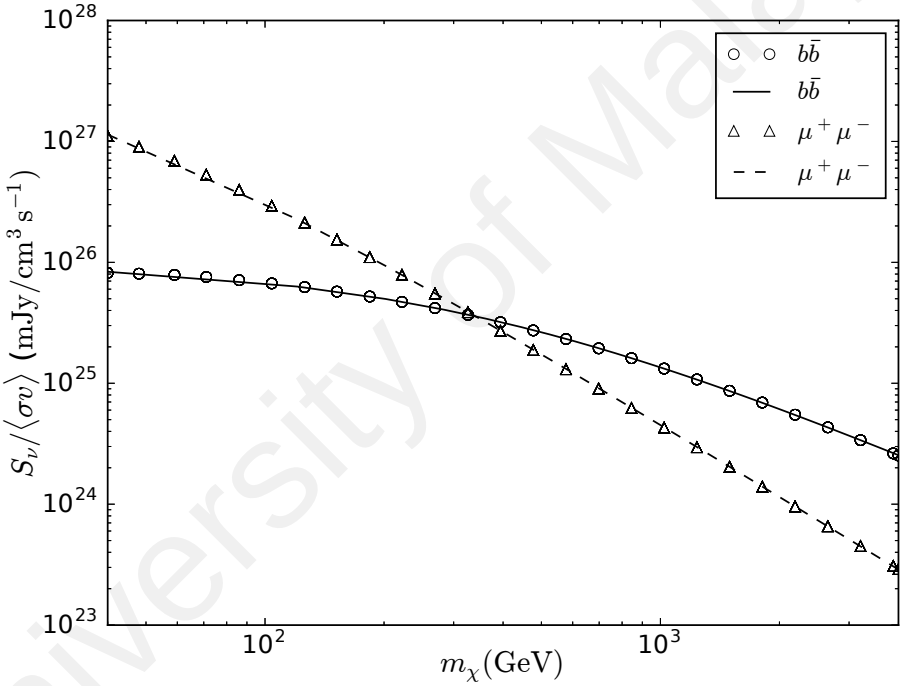

Figure 4.1: Plot of expected $S_{1.4\ \mathrm{GHz}}/\langle\sigma v\rangle$ versus m_χ from A1367, from 26×15 = 390 combinations of m_χ and $\langle\sigma v\rangle$, with annihilation through (circle) $b\bar{b}$ and (triangle) $\mu^+\mu^-$ channels. Solid and dashed curves are the fitting to S_ν–m_χ–$\langle\sigma v\rangle$ relation.

The observed diffuse radio emission (or its upper limit on detection) was interpreted as the maximum possible dark-matter-induced radio signal in the galaxy cluster. It was substituted into Equation (4.2) to obtain the upper limit constraint on $\langle\sigma v\rangle$–m_χ space. The corresponding $\langle\sigma v\rangle$–m_χ constraints are shown in Figure 4.2(a) for $b\bar{b}$ and 4.2(b) for $\mu^+\mu^-$. The horizontal band in the figure indicates the dark matter annihilation cross section that

Table 4.1: Fitting constants in S_ν–$\langle\sigma v\rangle$–m_χ relation. The uncertainty represents one standard deviation error from the fitting.

Cluster Name	$b\bar{b}$ Channel			
	c_1	c_2	c_3	χ^2
A1367	-1.414 ± 0.002	325 ± 1	29.545 ± 0.005	0.000139
Coma	-1.493 ± 0.001	72.7 ± 0.4	30.837 ± 0.004	0.000629
A2199	-1.504 ± 0.001	56.5 ± 0.4	30.097 ± 0.005	0.000565
2A0335	-1.441 ± 0.002	118.4 ± 0.7	28.586 ± 0.006	0.000550
A119	-1.451 ± 0.002	121.5 ± 0.6	29.336 ± 0.006	0.000451
A478	-1.441 ± 0.002	120.9 ± 0.7	28.434 ± 0.006	0.000538
Cluster Name	$\mu^+\mu^-$ **Channel**			
	c_1	c_2	c_3	χ^2
A1367	-2.0119 ± 0.0007	25.6 ± 0.1	30.712 ± 0.002	0.000206
Coma	-1.99930 ± 0.00003	4.980 ± 0.004	31.3685 ± 0.0001	1×10^{-6}
A2199	-1.99907 ± 0.00004	4.205 ± 0.004	30.5551 ± 0.0001	1×10^{-6}
2A0335	-1.99961 ± 0.00007	9.680 ± 0.008	29.4224 ± 0.0002	2×10^{-6}
A119	-1.99993 ± 0.00007	9.015 ± 0.009	30.1272 ± 0.0002	2×10^{-6}
A478	-1.99978 ± 0.00007	9.700 ± 0.009	29.2697 ± 0.0002	3×10^{-6}

would lead to the correct amount of dark matter relic abundance today (Equation 2.1). The CMB result from Planck Collaboration (2016) suggests $\Omega_\chi h^2 = 0.1186 \pm 0.0020$, which implies $\langle\sigma v\rangle/(1 \times 10^{-26}\ \mathrm{cm^3\ s^{-1}}) = [2.49, 2.57]$ and is within the allowed $\langle\sigma v\rangle$–m_χ range here. However, it also infers that if the particle is to be accounted for the relic abundance of dark matter observed today, its $\langle\sigma v\rangle$ will be too small to be fully responsible for the diffuse radio emission in galaxy clusters used in this study.

The constraints in Figure 4.2 are tighter in lower m_χ region. In other words, the expected synchrotron flux density decreases with increasing m_χ. In fact, a high mass neutralino annihilation yields more electrons at all energies than the low mass one does, therefore it should always lead to a higher synchrotron emissivity (see Figure 4.6 in Section 4.2.2). However, despite this positive correlation, the total synchrotron flux density here shows an opposite trend with m_χ. This is because the high dark matter particle mass reduces the dark matter number density in the galaxy cluster. This drop in dark matter number density overshadows the increase in synchrotron emissivity, leading to a relatively poor constraint at high m_χ.

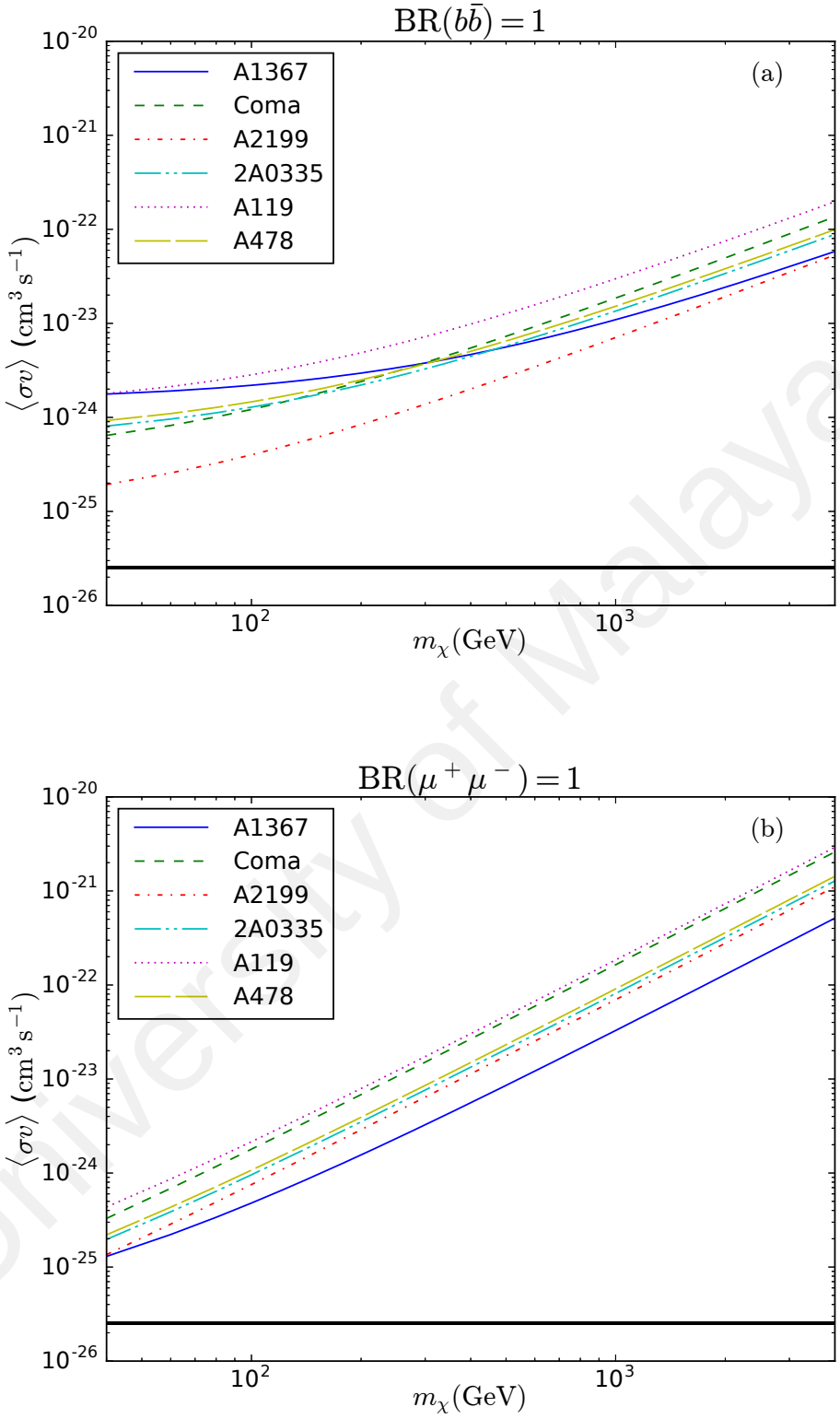

Figure 4.2: Upper limit constraints on $\langle\sigma v\rangle$–m_χ space with neutralino annihilation through (a) $b\bar{b}$ and (b) $\mu^+\mu^-$ channels. Horizontal band represents the range of $\langle\sigma v\rangle$ that would give the right amount of cosmological relic abundance of dark matter as seen by Planck Collaboration (2016).

Within the sample, the best constraints are derived from cluster A2199 for the $b\bar{b}$ channel and A1367 for the $\mu^+\mu^-$ channel (best in the sense that it constrains the largest $\langle\sigma v\rangle$–m_χ space among the sample). The constraint from A1367 has a different slope from other clusters: in terms of emissivity, it rises more with m_χ as compared to other clusters. This study has verified that it is not due to the dark matter distribution of A1367, but its magnetic field. The fact that A1367 has the lowest (though assumed) B_0 among the sample caused its emissivity to be most influenced by m_χ (see Section 4.2.2 and Figure 4.7 for more discussion on magnetic field).

Figure 4.2 also shows that the $\langle\sigma v\rangle$–m_χ constraint from $b\bar{b}$ channel is stronger than the constraint from $\mu^+\mu^-$ channel at high m_χ; while the opposite is true for low m_χ. This is due to the fact that $b\bar{b}$ channel would generate high differential yield of electrons at low energy, but falls quickly as energy approaches the dark matter particle mass limit; while $\mu^+\mu^-$ channel dominates at high energy instead. For example, under a $B_0 = 1$ μG environment, most of the synchrotron emission at 1.4 GHz is contributed by electrons with energy ≈ 19 GeV (the electron kinetic energy $K.E.$ that contributes maximally to a synchrotron emission at frequency ν can be estimated from the equation below (Longair, 2011)).

$$\nu \approx 3.7 \text{ MHz} \times \left(\frac{B}{1 \text{ μG}}\right) \times \left(\frac{K.E.}{1 \text{ GeV}}\right)^2 \tag{4.3}$$

At $K.E. = 19$ GeV, the 1000 GeV neutralino annihilation produces more electrons through $b\bar{b}$ channel than $\mu^+\mu^-$ channel. For a 40 GeV neutralino annihilation, however, $\frac{dN}{dE}^{b\bar{b}}$ falls below $\mu^+\mu^-$ channel because it is approaching the mass limit $E = m_\chi = 40$ GeV (Figure 3.6). Hence, the $\mu^+\mu^-$ channel is better constrained at low m_χ.

For the same reason, it is expected that the $b\bar{b}$ channel is better constrained than the $\mu^+\mu^-$ channel if one tries to derive the constraints with low-frequency radio observation (e.g., $\nu < 0.027$ GHz). On the other hand, for the observations with $\nu > 156$ GHz, the $\mu^+\mu^-$ channel will be better constrained since the channel has much higher $\frac{dN}{dE}$ than $b\bar{b}$ channel at high m_χ.

4.1.1 Comparison to Other Study

It is noted that Storm et al. (2013) (hereafter Storm13) had included A2199 in their constraint on $\langle\sigma v\rangle$–m_χ space. The constraint from A2199 in this study is a factor of 1.7 better than that of the authors – or equivalently, the expected S_ν here is 1.7 times higher than Storm13.

The derivation of expected S_ν used in this study is different from Storm13 in three ways: (1) the adopted cluster mass reconstruction method, (2) the spatial integration of emissivity, and (3) the construction of synchrotron emissivity ϵ_ν. The first factor boosts up S_ν in this study; while the other two tend to reduce S_ν as compared to Storm13. The three factors are discussed as follows.

4.1.1.1 Cluster Mass Reconstruction Method

Storm13 determined the M_{vir} of A2199 from the X-ray observation data of (Chen et al., 2007), and then derived c_{vir} by using the empirical X-ray M_{vir}–c_{vir} relation from (Buote et al., 2007) ($c_{vir} = 9\left(\frac{M_{vir}}{10^{14}h^{-1}M_\odot}\right)^{-0.172}$) ; while this study made use of M_{vir} and c_{vir} determined from the LOSVD measurement on the cluster (Łokas et al., 2006). In fact, the power-law index of the M_{vir}–c_{vir} relation is yielded differently for different mass reconstruction techniques. Furthermore, the X-ray mass reconstruction technique is based on the assumption of hydrostatic equilibrium, however, it is very common that this assumption is violated.

Within the radius of A2199 radio halo (or more specifically, the radius within which the upper limit on radio halo was determined), the LOSVD measurement gives a total mass of $M_{R\leq 500\ \mathrm{kpc,LOSVD}} = 2.31 \times 10^{14}\ \mathrm{M}_{\odot}$, which is 1.64 times higher than that of Storm13. This factor is considered together with the spatial integration of ϵ_ν in Section 4.1.1.2.

The uncertainty in the constraints derived using other mass reconstruction methods is further discussed in Section 4.2.

4.1.1.2 Spatial Integration of Emissivity

In the estimation of S_ν here, the spatial integration of ϵ_ν was performed over the spherical volume, instead of along the line-of-sight (l.o.s.) as Storm13 did. Since the calculation of S_ν is separable into particle-physics and astrophysics dependent terms, the astrophysics-dependent quantities can be compared by integrating the r-dependent properties over (1) l.o.s. and (2) spherical volume, as below.

$$J_{l.o.s.} = \int d\Omega \int_{l.o.s.} \rho^2(r) \frac{1}{B(r)} dl \tag{4.4}$$

$$J_{vol} = \frac{1}{{D_L}^2} \int_R r^2 \rho^2(r) \frac{1}{B(r)} dr \tag{4.5}$$

Note that $B(r)$ appeared as a denominator in the integration because of the B-dependence of b_{syn} in Equation (3.11.1).

The ratio between $J_{l.o.s.}$ and J_{vol} depends on the profile used. To compare between the astrophysical quantities assumed by Storm13 and this study, Equation (4.4) was evaluated with the NFW parameter assumed by Storm13; while Equation (4.5) was calculated with the NFW parameter listed in Table 3.2. As a result, $J_{l.o.s.}$ gave $1.68 \times 10^{21}\ \mathrm{GeV}^2\ \mathrm{cm}^{-5}$; while J_{vol} gave $2.39 \times 10^{21}\ \mathrm{GeV}^2\ \mathrm{cm}^{-5}$ – the spatial integration and mass reconstruction method adopted here together yielded S_ν a factor of 1.4 higher than Storm13.

4.1.1.3 Construction of Synchrotron Emissivity

Note that this study followed the approach in (Sarazin, 1999) to derive the synchrotron emissivity; whereas Storm13 adopted that of (Longair, 2011). One thing to note is that Storm13 used an approximation in the evaluation of the integral of the modified Bessel function. This approximation produces a synchrotron spectrum slightly different from Sarazin's approach. Figure 4.3 shows the synchrotron power at 0.327 GHz emitted from a single electron, evaluated at different energy, in the center of A2199, by using Sarazin's and Storm13's approach. Storm13's approach produces a higher synchrotron power especially at high energy and the energy that corresponds to the maximum emission.

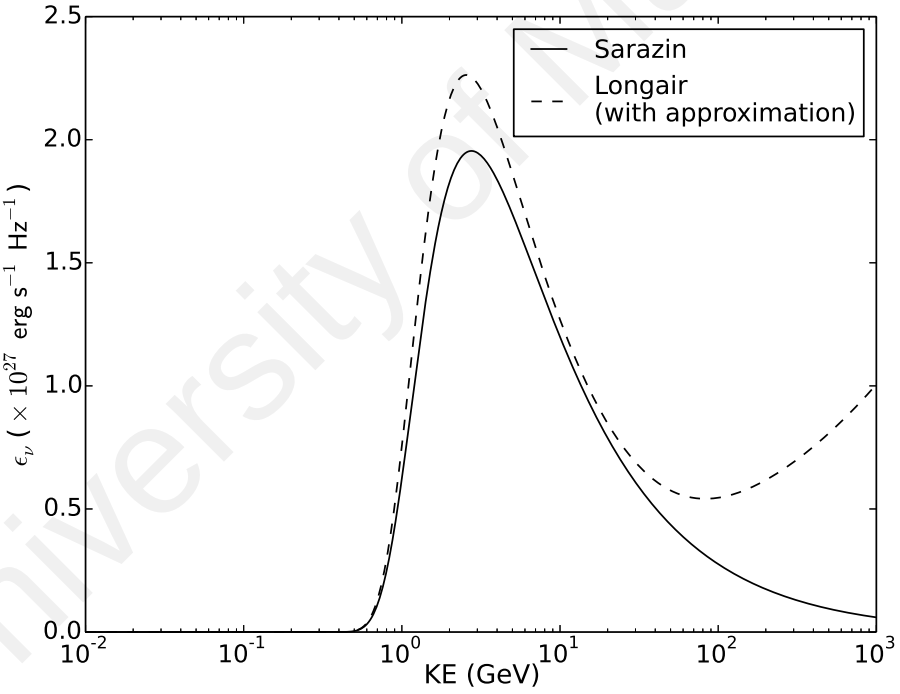

Figure 4.3: Synchrotron power per unit frequency from single electron at 0.327 GHz, evaluated at different energy, in the center of A2199.

In the environment of a galaxy cluster, the electron does not stay alone but comes in group. With the use of $\frac{dN}{dE}^{b\bar{b}}$ from 40 GeV dark matter particle annihilation (Figure 3.6), $S_{0.327\ \mathrm{GHz}}$ was estimated using both Sarazin's (solid line in Figure 4.3) and Storm13's approaches (dash line in Figure 4.3), from A2199 within r =500 kpc. It is found that

Storm13's method tends to produce S_v with a factor of 1.19 times higher than Sarazin's approach.

4.2 Uncertainty on the Constraint

In this section, the uncertainties on $\langle\sigma v\rangle$–m_χ space due to (1) mass reconstruction techniques and (2) intracluster magnetic field are discussed.

4.2.1 Mass Reconstruction Techniques

The c_{vir} and M_{vir} derived from different mass reconstruction techniques do not come to a good agreement, it varies depending on the reconstruction method (Groener et al., 2016).

In this section, the dark matter density profile of A2199 (and hence its $\langle\sigma v\rangle$–m_χ constraint) was re-derived, using other mass reconstruction techniques (e.g., CM, LOSVD, and X-ray), with the values of c_{vir} and M_{vir} taken from Table A1 of (Groener et al., 2016) and re-listed here again in Table 4.2 for the ease of reference. The re-derived constraints from $b\bar{b}$ channel are shown in Figure 4.4. Note that the constraint with legend 'Storm13' does not represent their result, only their NFW parameters were adopted in here. The best constraint (Xray14) is a factor of 7 better than the poorest constraint (CM06) – the uncertainty in c_{vir} and M_{vir} led to nearly one order of magnitude in the uncertainty of $\langle\sigma v\rangle$–m_χ constraint.

Table 4.2: Other NFW parameters of A2199.

Label	**Method**	c_{vir}	M_{vir}	**Reference**
-	-	-	10^{14} $M_\odot$	-
CM03	CM	9.8	5.47	(Rines et al., 2003)
CM06	CM	5.39	4.62	(Rines & Diaferio, 2006)
LOSVD06	LOSVD	10.4	7.1	(Łokas et al., 2006)
Xray14	X-ray	8.42	14.91	(Babyk et al., 2014)
Storm13	Storm13	7.48	4.18	(Storm et al., 2013)

Besides the exact values of c_{vir} and M_{vir}, the dark matter substructure introduces another significant uncertainty in spatial distribution. Although this study did not consider any

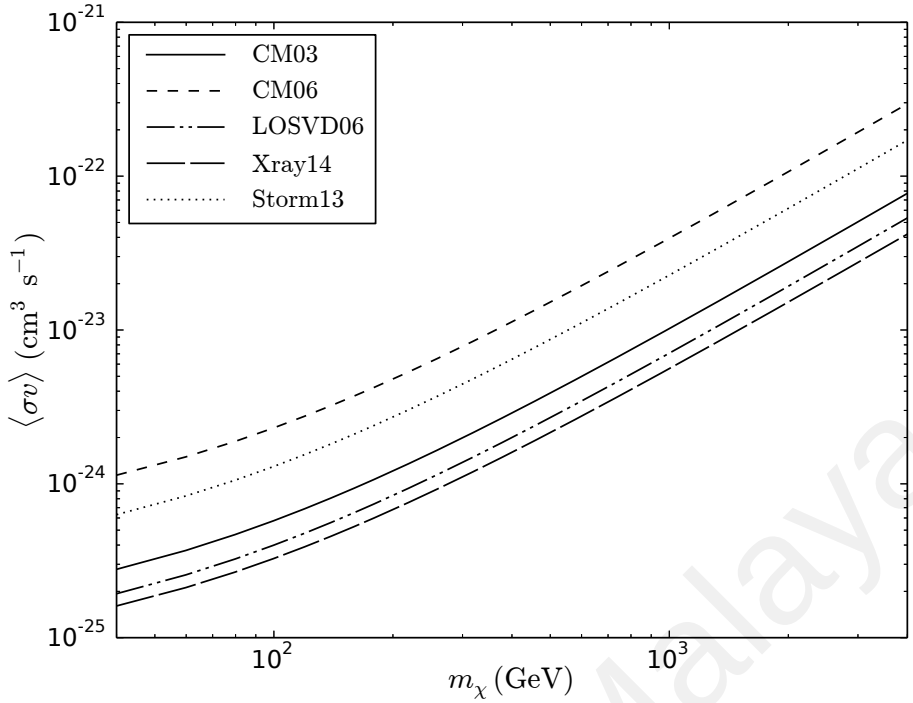

Figure 4.4: Re-derived upper limit constraints on $\langle \sigma v \rangle$–m_χ through $b\bar{b}$ channel annihilation, from cluster A2199, with density profiles determined using different mass reconstruction methods as listed in Table 4.2.

halo substructure, it is worth noting its existence. The numerical dark matter simulation shows substructures (and sub-substructures) in the dark matter haloes (Springel et al., 2008; Klypin et al., 2011). The substructure is expected to significantly increase the annihilation signal. Its influence is more dominant in the outer region of halo. The substructure can introduce a gain that is one order of magnitude higher than the smooth profile, depending highly on the substructure model.

4.2.2 Intracluster Magnetic Field

The intracluster magnetic field is one of the key components in producing the synchrotron emission. In this section, the uncertainty introduced by B_0 and η is discussed.

Five cases were assumed with B_0 between 5 to 40 μG (assuming $\eta = 1.0$) for the cluster 2A0335. The corresponding $\langle \sigma v \rangle$–m_χ constraints are shown in Figure 4.5. The figure shows that a high B_0 field does not necessarily guarantee a better constraint (or equivalently

a higher S_ν) from the dark matter. In the high m_χ region (the rectangular box in the figure), the constraints from B_0 = 40 and 30 μG are instead poorer than those from lower B_0 fields. This trend can also clearly be seen in the synchrotron emissivity shown in Figure 4.6.

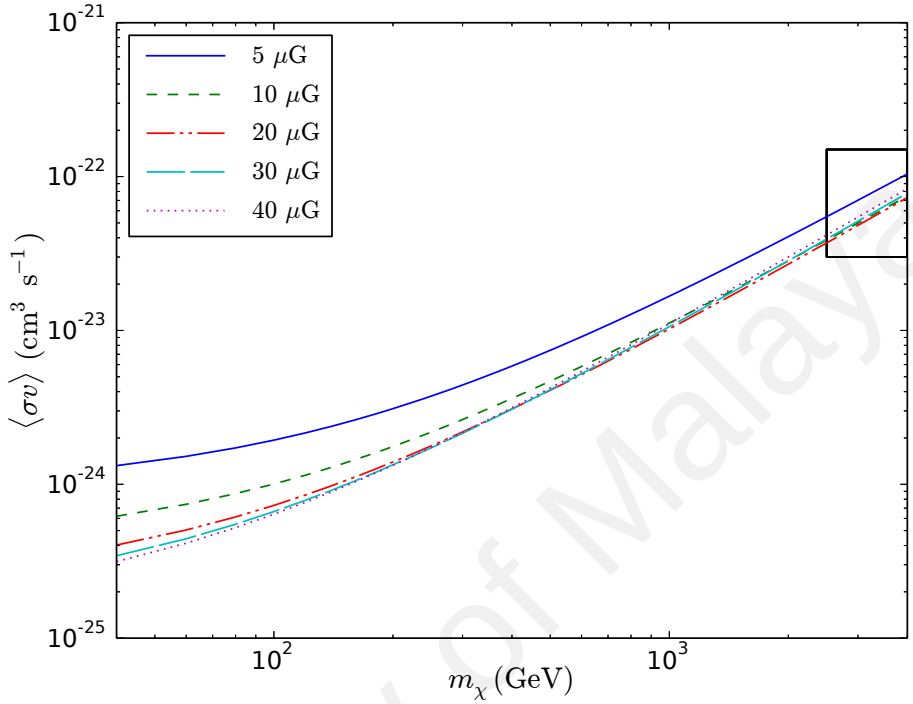

Figure 4.5: Upper limit constraints on $\langle\sigma v\rangle$–m_χ space through $b\bar{b}$ annihilation channel, from cluster 2A0335, with B_0 = 5, 10, 20, 30, and 40 μG assumed (and η = 0.5).

It is true that, for a single electron, the synchrotron emission at frequency ν increases together with B_0. In the environment of a galaxy cluster, however, one must consider the time-independent equilibrium state and various energy losses (Equation 3.11), the latter of which approximately increase with the square of B_0. In other words, while B_0 gets higher, the electrons lose more energy through other frequencies as a whole. Therefore, it is reasonable that the constraints from high B_0 fields are poorer than those from lower B_0 fields. The trend however is not seen in the constraints at lower m_χ, due to its steep electron spectrum. Note that the amount of high energy electrons produced from the low-mass neutralinos is far less than that from high-mass neutralinos; on the other hand, a

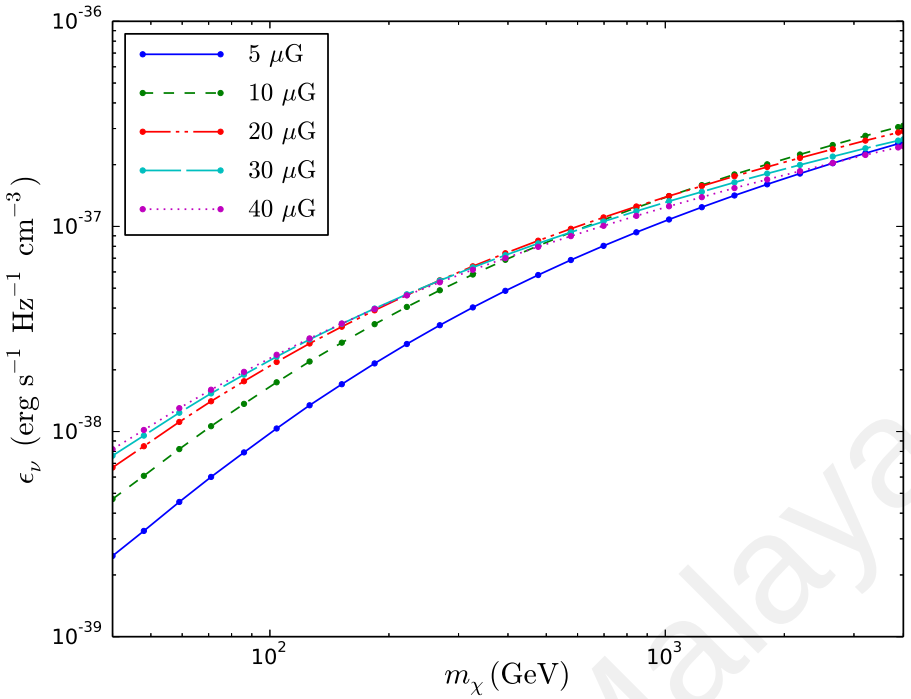

Figure 4.6: Synchrotron emissivity at 1.4 GHz versus m_χ (with $b\bar{b}$ annihilation channel assumed and $\langle\sigma v\rangle = 1.0 \times 10^{-26}$ cm^3 s^{-1}) under different B_0 environment, evaluated at r that corresponds to $N_\chi(r) = 1$ cm^{-3} in 2A0335.

lower magnetic field requires higher energy electrons to radiate synchrotron emission at fixed frequency ν. For low-mass neutralinos, there are too few electrons at high energy end to account for the emission at low B_0. The synchrotron emission is thus less efficient as magnetic field decreases – it behaves as if the synchrotron emission positively correlates with the magnetic field strength for a low mass neutralino.

In Figure 4.6, one thing to note is that the emissivity under a lower B_0 field rises more with m_χ as compared to those under a higher B_0 field. Figure 4.7 shows the electron equilibrium spectra from 40 and 4000 GeV neutralinos, under different B_0 environment. As shown in the figure, the gap between $n_{eq}(E)$ from different neutralino masses is not constant throughout the electron energy. It is large in the high energy end; while smaller and approaching constant in the low energy end. Under a low B_0 field, a high electron

energy is required for the emission. This is energy range where the gap between $n_{eq}(E)$ is relatively large (see the dashed arrow), and the low B_0 constraint is more influenced by m_χ.

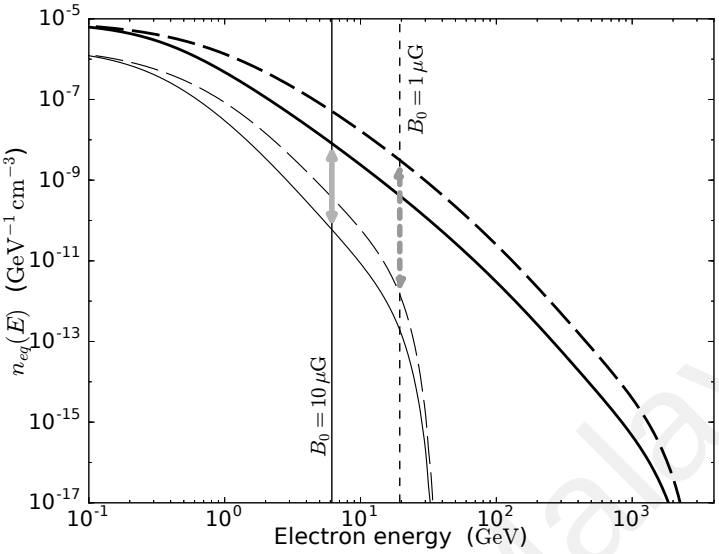

Figure 4.7: Electron equilibrium spectrum ($b\bar{b}$ channel and $\langle\sigma v\rangle = 1.0 \times 10^{-26}$ cm^3 s^{-1} assumed) under (dashed) $B_0 = 1$ μG and (solid) $B_0 = 10$ μG environment, evaluated at r that corresponds to $N_\chi(r) = 1$ cm^{-3} in 2A0335. Arrow indicates the difference between $n_{eq}(E)$ from 40 (thin) and 4000 GeV (thick) neutralinos. Vertical line: electron energy that contributes maximally to $S_{1.4\text{ GHz}}$.

In the results that have been obtained so far, $\eta = 1.0$ was assumed for the clusters without reports on their magnetic field properties. Here, the $\langle\sigma v\rangle$–m_χ constraint from 2A0335 (assuming $B_0 = 10$ μG) was re-derived at a different assumed η (= 0.5) (see Figure 4.8(a) for the profile). The constraints are compared in Figure 4.8(b). The $\eta = 0.5$ field yielded 30% higher $S_{1.4\text{GHz}}$ than a $\eta = 1.0$ field would do at $m_\chi = 40$ GeV; while only 18% higher at $m_\chi = 4000$ GeV.

4.3 Constraint on SUSY Parameter Space

As mentioned in the earlier chapter, in the mSUGRA and MSSM scenarios, the neutralino mass, $\langle\sigma v\rangle$, and BRs are determined by the combination of free parameters. The neutralino properties and electron spectrum obtained from parameter scanning were

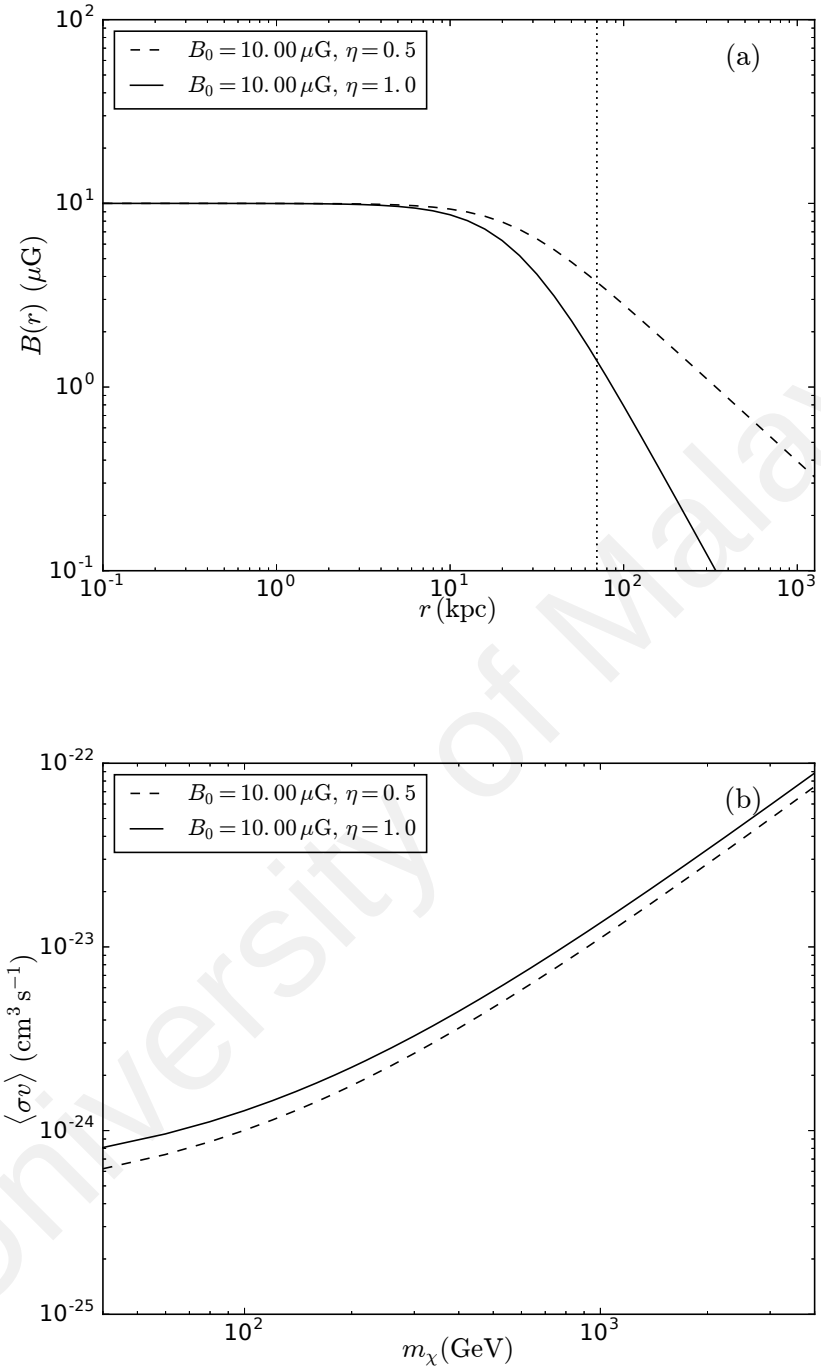

Figure 4.8: (a) Magnetic fields in galaxy cluster 2A0335 of different assumed η. Vertical dotted line indicates the radius of the mini halo. (b) Upper limit constraints on $\langle\sigma v\rangle$–m_χ space through $b\bar{b}$ annihilation channel, from cluster 2A0335 (assuming B_0 = 10 µG), at η = 0.5 and 1.0.

then used to derived the synchrotron flux density from dark matter. The results of scanning on the two models are discussed in this section.

All the calculations of S_ν in this section were made at $\nu = 0.327$ GHz, under the assumption of cluster A2199 with its properties listed in Table 3.2 and Table 3.3.

4.3.1 mSUGRA combinations

All the 5353 combinations of mSUGRA parameters from DARKSUSY scanning are shown in Appendix A.1, plotted in tan β and $m_{1/2}$ as x and y axes, with colour representing m_χ (and $S_{0.327\ \mathrm{GHz}}$ in Appendix A.2). The tick labels in x and y axes are the discrete values of the parameter scanning (tan β and $m_{1/2}$, respectively. See Table 3.5.). Since it is a multidimensional data, showing the combinations in only two axes will cause the combinations that have the same x and y values to overlay (e.g., any combinations that fulfil tan $\beta = 5$ and $m_{1/2} = 50$ GeV), appearing only as one point in the plot. For this reason, an offset was purposely created in their positions to avoid overlapping in the data representation, while the visible grouping of data (that share the same x and y values) was carefully maintained. In the figure, the combinations that share the same tan β and $m_{1/2}$ were slightly shifted (first level shifts) in x and y directions, with amount of shifting proportional to A_0 and m_0, respectively. The combinations that further share the same A_0 and m_0 but negative in sign(μ) were further shifted (second level shift, in a smaller amount) in the x direction again to avoid overlapping.

See Appendix C for how to read the mSUGRA combinations in Appendix A.1 and A.2 (and MSSM combinations in the next section).

The neutralino mass has a rather simple dependence on the parameters, mainly on $m_{1/2}$. On the other hand, the flux density does not have a simple scaling relation with the mSUGRA parameters, but combinations with higher tan β tend to produce higher synchrotron flux. The upper limit on diffuse radio emission detection in A2199 managed

to exclude 34 mSUGRA parameter combinations as they would produce S_ν higher than the observed upper limit. All the excluded mSUGRA combinations reside in high tan β region (tan β = 55 and 65) and have small neutralino mass ($m_\chi < 60$ GeV). Note that the earlier experimental search for neutralino put a lower limit on its mass ($m_\chi > 46$ GeV) (Patrignani et al. (Particle Data Group), 2016).

The ATLAS experiment placed limits on the parameters of mSUGRA model, but focused only on the $m_{1/2}$–m_0 space (ATLAS Collaboration, 2015). The results here show that m_0 does not have significant influence on synchrotron flux as $m_{1/2}$ does (through its influence on m_χ). Thus, this method is not preferable if one is interested in constraining the $m_{1/2}$–m_0 space.

4.3.2 MSSM combinations

The 20247 sets of MSSM combinations are shown in μ and M_2 axes, with colour representing m_χ in Appendix B.1 and S_ν in Appendix B.2, the latter of which is further split into four smaller regions and are shown separately in Appendix B.3–B.6. Since it is a six dimensional data, again, in order to avoid overlaying in the data representation, the combinations that share the same μ and M_2 were slightly shifted in x and y directions (first level shifts), with shifting proportional to m_0 and m_A, respectively. A (smaller and) second level shift in x and y directions were given to the data that further share the same m_0 and m_A, with shifting proportional to tan β and A_t/m_0, respectively.

In this scenario, the neutralino mass has a positive dependence on M_2 and μ; while the synchrotron flux has a rather complicated relation with the parameters. From Appendix B.1 and Appendix B.2, for those having neutralinos of same mass, a lower μ tends to produce higher synchrotron flux overall. The combinations that have neutralino mass and m_A approximately along $m_A = 2m_\chi + 42$ produce even higher synchrotron flux. The upper limit of radio observation on A2199 is able to exclude 482 MSSM combinations in

this study. Unlike the mSUGRA result where the excluded combinations come only from the combinations that produce the lowest possible m_χ among the scanning sample, the neutralino mass from the excluded MSSM combinations cover some higher m_χ combinations as well (≈170, 320, and 620 GeV). All the excluded combinations are along the $m_A = 2m_\chi + 42$ relation.

4.4 Constraint on Kaluza-Klein Dark Matter

The final section of this analysis chapter puts a constraint on the LKP. The constraint on $B^{(1)}$ was derived in the same way as for the single channel neutralino annihilation, but with branching ratio in Table 3.6 adopted instead. Synchrotron emission was computed at $\nu = 0.327$ GHz, under the same cluster environment as used in Section 4.3. The constraint is shown in Figure 4.9, plotted along with the neutralino $b\bar{b}$ and $\mu^+\mu^-$ channels for comparison. The expected S_ν at different frequencies were computed as well for the two types of dark matter particles (both assuming 800 GeV dark matter particle mass and $\langle\sigma v\rangle = 1.0 \times 10^{-26}$ cm^3 s^{-1}) and are shown in Figure 4.10. Both the $B^{(1)}$ constraint and its the synchrotron spectrum fall between the constraints from neutralino extreme channels. Although $B^{(1)}$ has a distinctive signature at the high energy end of its electron spectrum, the signature is not prominent in radio synchrotron spectrum.

In fact, in UED, there is an analytical relation between $\langle\sigma v\rangle$ and $m_{B^{(1)}}$: $\sigma v \simeq 3 \times 10^{-26}(0.8 \text{ TeV}/m_{B^{(1)}})^2 \text{ cm}^3 \text{ s}^{-1}$ (Servant & Tait, 2003). This analytical relation is shown as the thick line in the bottom of Figure 4.9. It is within the upper limit constraint, implying again that $B^{(1)}$ annihilation can only contribute very little to the diffuse radio emission. A much higher observation sensitivity (two to three orders better) is required if one would like to test this relation through synchrotron mechanism.

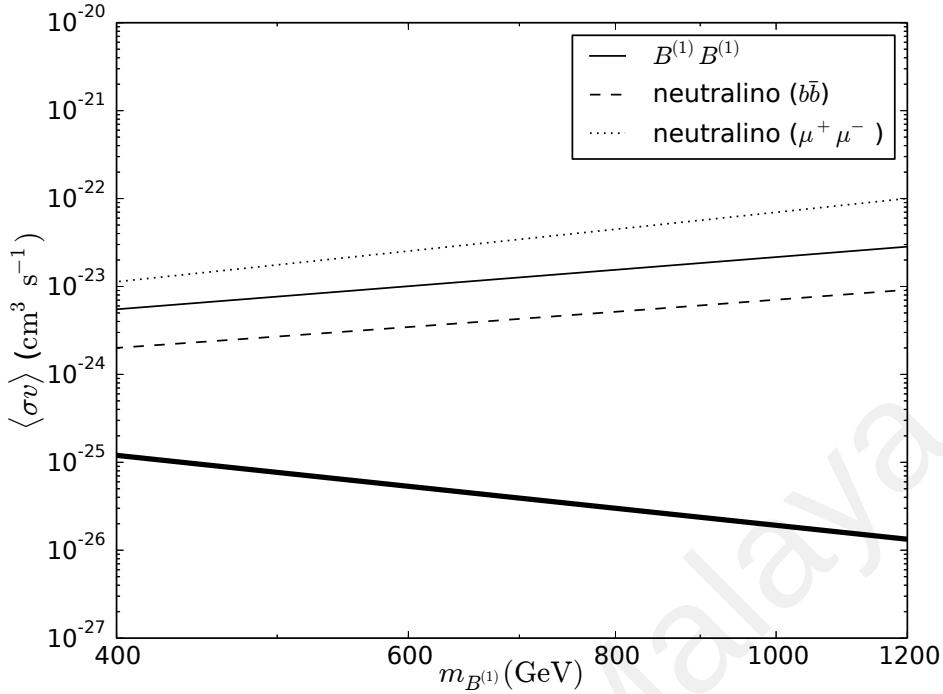

Figure 4.9: Constraint on $B^{(1)}$ by using the upper limit on radio halo detection from A2199 at 0.327 GHz. Thick solid line at the bottom shows the analytical $m_{B^{(1)}}$–$\langle\sigma v\rangle$ relation.

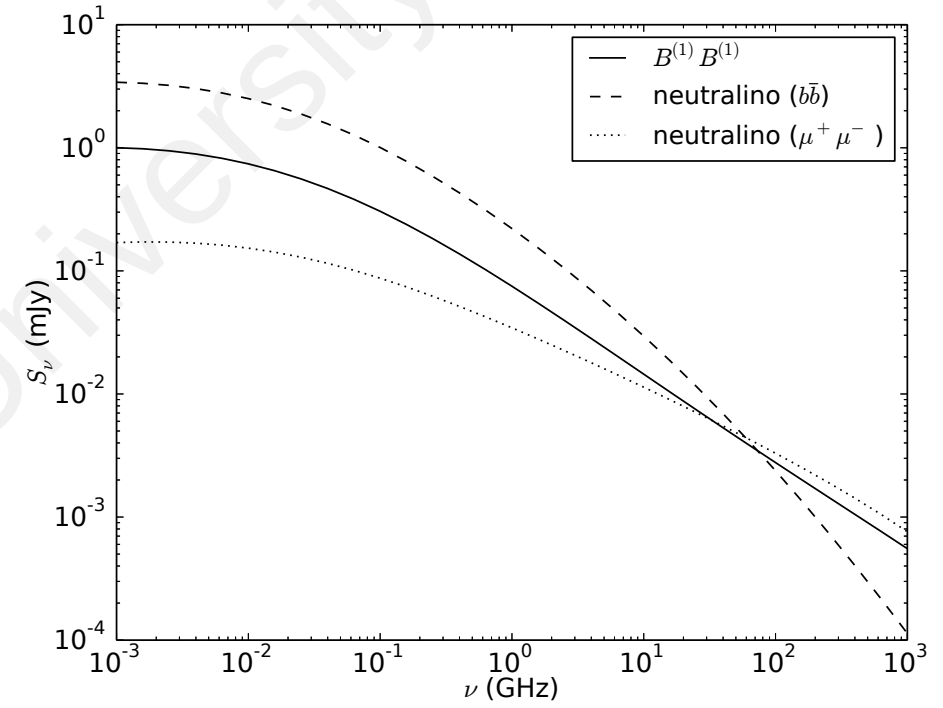

Figure 4.10: Expected synchrotron flux density computed at different frequency, from the dark matter in A2199 within a radius of 500 kpc (assuming 800 GeV dark matter particle mass and $\langle\sigma v\rangle = 1.0 \times 10^{-26}$ cm^3 s^{-1}).

CHAPTER 5: SUMMARY AND CONCLUSIONS

5.1 Conclusions

This study constrained the properties of WIMP dark matter (the LSP and LKP) by interpreting the diffuse radio emission (or its upper limit on detection) as the maximum possible synchrotron emission induced by dark matter annihilation. The results are summarized as follows.

- The upper limit constraint on WIMP $\langle\sigma v\rangle$–m_χ space has been derived, for m_χ between 40 and 4000 GeV, through the extreme fundamental channels ($b\bar{b}$ and $\mu^+\mu^-$). The results are comparable to the constraints derived by other study.

- If the WIMP is to be accounted for the relic abundance of dark matter observed today, its annihilation cross section will be too small to reproduce the diffuse radio emission in the sample galaxy clusters used in this study. Nevertheless, the WIMP dark matter can still contribute to the diffuse radio emission in smaller percentage.

- Constraints on parameter space have been set for the mSUGRA and phenomenological MSSM models in DARKSUSY. The excluded parameter combinations have been shown. For mSUGRA, this method is good in constraining the high $\tan\beta$ ($\gtrsim 55$) and low m_χ ($\lesssim 60$ GeV), but not suitable in constraining the $m_{1/2}$–m_0 space. For the case of MSSM, the dark matter from parameter combinations lying approximately along $m_A = 2m_\chi + 42$ tend to produce synchrotron emission that is too high to explain the diffuse radio emission.

- It is hard to distinguish the KK dark matter ($B^{(1)}$) from the SUSY neutralino by simply looking at the synchrotron spectrum in radio frequency.

- If $B^{(1)}$ is the main component of dark matter and follows its analytical $\langle\sigma v\rangle$–$m_{B^{(1)}}$ relation, it will not be fully responsible for the diffuse radio emission in the sample galaxy cluster considered here.

- A much higher sensitivity (two to three orders) radio observation is required if one would like to use the diffuse radio emission to test the analytical $B^{(1)}$ $\langle\sigma v\rangle$–$m_{B^{(1)}}$ relation.

- The uncertainties on constraint due to cluster mass reconstruction and magnetic field have been identified. The largest uncertainty comes from the former.

- A stronger magnetic field does not always produce a higher synchrotron emission (or equivalently a better constraint). In order to achieve a good constraint, the best target to choose is the galaxy cluster that does not hold any diffuse radio emission.

5.2 Significance of Research

This research is a "hybrid" of particle physics and astrophysics. It approaches the dark matter problem from the astrophysics aspect (the indirect detection). The results from this study have provided a bound on the large parameter space of the physics beyond the SM. It is possible that one extends this research to a number of studies related to the origin of diffuse radio emission in galaxy cluster.

5.3 Recommendations for Future Research

A few recommendations are suggested for future research, as listed below.

- The constraint derived in this study was based on the comparison made between the expected and observed emission at only one frequency. In fact, the synchrotron spectrum spans a wide range of frequency. A multifrequency analysis is highly recommended for future study.

- This study made use of only the magnitude of overall synchrotron flux density from the whole cluster volume, without looking at the morphology of the emission. It would be good if one can include the morphology of emission in future analysis.

- Besides the synchrotron mechanism, the relativistic electrons also lose their energy through the inverse-Compton scattering process, which could scatter the CMB to gamma-ray range. It is worth exploring the dark matter constraints using the gamma-ray data.

REFERENCES

Abazajian, K. N., Canac, N., Horiuchi, S., & Kaplinghat, M. (2014). Astrophysical and dark matter interpretations of extended gamma-ray emission from the Galactic Center. *Physical Review D: Particles and Fields*, *90*, 023526.

Abramowski, A., Aharonian, F., Ait Benkhali, F., Akhperjanian, A. G., Angüner, E. O., Backes, M., . . . Zechlin, H.-S. (2015). Constraints on an annihilation signal from a core of constant dark matter density around the Milky Way Center with H.E.S.S. *Physical Review Letters*, *114*, 081301.

Accardo, L., Aguilar, M., Aisa, D., Alpat, B., Alvino, A., Ambrosi, G., . . . Zurbach, C. (2014). High statistics measurement of the positron fraction in primary cosmic rays of 0.5-500 GeV with the Alpha Magnetic Spectrometer on the International Space Station. *Physical Review Letters*, *113*, 121101.

Ackermann, M., Ajello, M., Allafort, A., Atwood, W. B., Baldini, L., Barbiellini, G., . . . Zimmer, S. (2012). Measurement of separate cosmic-ray electron and positron spectra with the Fermi Large Area Telescope. *Physical Review Letters*, *108*, 011103.

Ackermann, M., Ajello, M., Allafort, A., Baldini, L., Ballet, J., Barbiellini, G., . . . Roth, M. (2010). Constraints on dark matter annihilation in clusters of galaxies with the Fermi large area telescope. *Journal of Cosmology and Astroparticle Physics*, *2010*(05), 025.

Adriani, O., Barbarino, G. C., Bazilevskaya, G. A., Bellotti, R., Boezio, M., Bogomolov, E. A., . . . Zverev, V. G. (2009). An anomalous positron abundance in cosmic rays with energies 1.5–100 GeV. *Nature*, *458*, 607–609.

Agnes, P., Alexander, T., Alton, A., Arisaka, K., Back, H., Baldin, B., . . . Yoo, J. (2015). First results from the DarkSide-50 dark matter experiment at Laboratori Nazionali del Gran Sasso. *Physics Letters B*, *743*, 456–466.

Aguilar, M., Alberti, G., Alpat, B., Alvino, A., Ambrosi, G., Andeen, K., . . . Zurbach, C. (2013). First result from the Alpha Magnetic Spectrometer on the International Space Station: Precision measurement of the positron fraction in primary cosmic rays of 0.5–350 GeV. *Physical Review Letters*, *110*, 141102.

Allen, S. W., Schmidt, R. W., Ebeling, H., Fabian, A. C., & van Speybroeck, L. (2004). Constraints on dark energy from Chandra observations of the largest relaxed galaxy clusters. *Monthly Notices of the Royal Astronomical Society*, *353*, 457–467.

Appelquist, T., Cheng, H.-C., & Dobrescu, B. A. (2001). Bounds on universal extra dimensions. *Physical Review D: Particles and Fields*, *64*, 035002.

Arkani-Hamed, N., Dimopoulos, S., & Dvali, G. (1999). Phenomenology, astrophysics, and cosmology of theories with submillimeter dimensions and TeV scale quantum gravity. *Physical Review D: Particles and Fields*, *59*, 086004.

ATLAS Collaboration. (2015). Summary of the searches for squarks and gluinos using $\sqrt{s}$ = 8 TeV *pp* collisions with the ATLAS experiment at the LHC. *Journal of High Energy Physics*, *2015*(10), 54.

ATLAS Collaboration. (2016). Search for new phenomena in final states with an energetic jet and large missing transverse momentum in *pp* collisions at $\sqrt{s}$ = 13 TeV using the ATLAS detector. *Physical Review D: Particles and Fields*, *94*, 032005.

Babyk, Y. V., Del Popolo, A., & Vavilova, I. B. (2014). Chandra X-ray galaxy clusters at $z < 1.4$: Constraints on the inner slope of the density profiles. *Astronomy Reports*, *58*(9), 587–610.

Bagchi, J., Durret, F., Neto, G. B. L., & Paul, S. (2006). Giant ringlike radio structures around galaxy cluster Abell 3376. *Science*, *314*, 791–794.

Bai, Y., Fox, P. J., & Harnik, R. (2010). The Tevatron at the frontier of dark matter direct detection. *Journal of High Energy Physics*, *2010*(12), 48.

Baltz, E. A., Berenji, B., Bertone, G., Bergström, L., Bloom, E., Bringmann, T., ... Winer, B. L. (2008). Pre-launch estimates for GLAST sensitivity to dark matter annihilation signals. *Journal of Cosmology and Astroparticle Physics*, *2008*(07), 013.

Bennett, C. L., Larson, D., Weiland, J. L., Jarosik, N., Hinshaw, G., Odegard, N., ... Wollack, E. (2013). Nine-year Wilkinson Microwave Anisotropy Probe (WMAP) observations: Final maps and results. *The Astrophysical Journal Supplement Series*, *208*, 20.

Bernabei, R., Belli, P., Cappella, F., Caracciolo, V., Castellano, S., Cerulli, R., . . . Ye, Z. P. (2015). Final model independent results of DAMA/LIBRA–Phase1 and perspectives of Phase2. *Physics of Particles and Nuclei*, *46*, 138–146.

Bhupal Dev, P. S., Ghosh, D. K., Okada, N., & Saha, I. (2014). Neutrino mass and dark matter in light of recent AMS-02 results. *Physical Review D: Particles and Fields*, *89*, 095001.

Blasi, P., & Colafrancesco, S. (1999). Cosmic rays, radio halos and nonthermal X-ray emission in clusters of galaxies. *Astroparticle Physics*, *12*, 169–183.

Bonafede, A., Feretti, L., Murgia, M., Govoni, F., Giovannini, G., Dallacasa, D., . . . Taylor, G. B. (2010). The Coma cluster magnetic field from Faraday rotation measures. *Astronomy and Astrophysics*, *513*, A30.

Bonafede, A., Giovannini, G., Feretti, L., Govoni, F., & Murgia, M. (2009). Double relics in Abell 2345 and Abell 1240. Spectral index and polarization analysis. *Astronomy and Astrophysics*, *494*, 429–442.

Boyarsky, A., Malyshev, D., & Ruchayskiy, O. (2011). A comment on the emission from the Galactic Center as seen by the Fermi telescope. *Physics Letters B*, *705*, 165–169.

Briel, U. G., Henry, J. P., & Böhringer, H. (1992). Observation of the Coma cluster of galaxies with ROSAT during the All-Sky Survey. *Astronomy and Astrophysics*, *259*, L31–L34.

Brown, S., & Rudnick, L. (2011). Diffuse radio emission in/around the Coma cluster: beyond simple accretion. *Monthly Notices of the Royal Astronomical Society*, *412*, 2–12.

Brunetti, G., Setti, G., & Giovannini, L. F. G. (2001). Particle reacceleration in the Coma cluster: radio properties and hard X-ray emission. *Monthly Notices of the Royal Astronomical Society*, *320*, 365–378.

Brunetti, G., Venturi, T., Dallacasa, D., Cassano, R., Dolag, K., Giacintucci, S., & Setti, G. (2007). Cosmic rays and radio halos in galaxy clusters: New constraints from radio observations. *Astrophysical Journal*, *670*, L5–L8.

Bryan, G. L., & Norman, M. L. (1998). Statistical properties of X-ray clusters: Analytic and numerical comparisons. *Astrophysical Journal*, *495*, 80–99.

Buchmueller, O., Malik, S. A., McCabe, C., & Penning, B. (2015). Constraining dark matter interactions with pseudoscalar and scalar mediators using collider searches for multijets plus missing transverse energy. *Physical Review Letters*, *115*, 181802.

Bullock, J. S., Kolatt, T. S., Sigad, Y., Somerville, R. S., Kravtsov, A. V., Klypin, A. A., ... Dekel, A. (2001). Profiles of dark haloes: evolution, scatter and environment. *Monthly Notices of the Royal Astronomical Society*, *321*, 559–575.

Buote, D. A., Gastaldello, F., Humphrey, P. J., Zappacosta, L., Bullock, J. S., Brighenti, F., & Mathews, W. G. (2007). The X-ray concentration-virial mass relation. *Astrophysical Journal*, *664*, 123–134.

Burkert, A. (1995). The structure of dark matter halos in dwarf galaxies. *Astrophysical Journal*, *447*, L25–L28.

Caputo, R., Buckley, M. R., Martin, P., Charles, E., Brooks, A. M., Drlica-Wagner, A., ... Wood, M. (2016). Search for gamma-ray emission from dark matter annihilation in the Small Magellanic Cloud with the Fermi Large Area Telescope. *Physical Review D: Particles and Fields*, *93*, 062004.

Carilli, C. L., & Taylor, G. B. (2002). Cluster magnetic fields. *Annual Review of Astronomy and Astrophysics*, *40*, 319–348.

Cassano, R., Brunetti, G., Venturi, T., Setti, G., Dallacasa, D., Giacintucci, S., & Bardelli, S. (2008). Revised statistics of radio halos and the reacceleration model. *Astronomy and Astrophysics*, *480*, 687–697.

Cassano, R., Ettori, S., Giacintucci, S., Brunetti, G., Markevitch, M., Venturi, T., & Gitti, M. (2010). On the connection between giant radio halos and cluster mergers. *The Astrophysical Journal Letters*, *721*, L82–L85.

Chang, J., Adams Jr, J. H., Ahn, H. S., Bashindzhagyan, G. L., Christl, M., Ganel, O., ... Zatsepin, V. I. (2008). An excess of cosmic ray electrons at energies of 300 – 800 GeV. *Nature*, *456*, 362–365.

Chen, Y., Reiprich, T. H., Böhringer, H., Ikebe, Y., & Zhang, Y.-Y. (2007). Statistics of X-ray observables for the cooling-core and non-cooling core galaxy clusters. *Astronomy and Astrophysics*, *466*, 805–812.

Cheng, H.-C., Matchev, K. T., & Schmaltz, M. (2002). Radiative corrections to Kaluza-Klein masses. *Physical Review D: Particles and Fields*, *66*, 036005.

Cholis, I., & Hooper, D. (2013). Dark matter and pulsar origins of the rising cosmic ray positron fraction in light of new data from the AMS. *Physical Review D: Particles and Fields*, *88*, 023013.

CMS Collaboration. (2015). Search for dark matter, extra dimensions, and unparticles in monojet events in proton-proton collisions at $\sqrt{s}$=8 TeV. *The European Physical Journal C*, *75*, 235.

CMS Collaboration. (2017). Search for dijet resonances in proton–proton collisions at $\sqrt{s}$=13 TeV and constraints on dark matter and other models. *Physics Letters B*, *769*, 520–542.

Colafrancesco, S., & Mele, B. (2001). Neutralinos and the origin of radio halos in clusters of galaxies. *Astrophysical Journal*, *562*, 24–41.

Comerford, J. M., & Natarajan, P. (2007). The observed concentration-mass relation for galaxy clusters. *Monthly Notices of the Royal Astronomical Society*, *379*, 190–200.

Cuciti, V., Cassano, R., Brunetti, G., Dallacasa, D., Kale, R., Ettori, S., & Venturi, T. (2015). Occurrence of radio halos in galaxy clusters. Insight from a mass-selected sample. *Astronomy and Astrophysics*, *580*, A97.

de Gasperin, F., Intema, H. T., van Weeren, R. J., Dawson, W. A., Golovich, N., Wittman, D., ... Brüggen, M. (2015). A powerful double radio relic system discovered in PSZ1 G108.18-11.53: evidence for a shock with non-uniform Mach number? *Monthly Notices of the Royal Astronomical Society*, *453*, 3483–3498.

Dennison, B. (1980). Formation of radio halos in clusters of galaxies from cosmic-ray protons. *Astrophysical Journal*, *239*, L93–L96.

Diemand, J., Zemp, M., Moore, B., Stadel, J., & Carollo, M. (2005). Cusps in cold dark matter haloes. *Monthly Notices of the Royal Astronomical Society*, *364*, 665–673.

Dolag, K., & Enßlin, T. A. (2000). Radio halos of galaxy clusters from hadronic secondary electron injection in realistic magnetic field configurations. *Astronomy and Astrophysics*, *362*, 151–157.

Dolag, K., Schindler, S., Govoni, F., & Feretti, L. (2001). Correlation of the magnetic field and the intra-cluster gas density in galaxy clusters. *Astronomy and Astrophysics*, *378*, 777–786.

Eckert, D., Molendi, S., & Paltani, S. (2011). The cool-core bias in X-ray galaxy cluster samples I. Method and application to HIFLUGCS. *Astronomy and Astrophysics*, *526*, A79.

Ellis, J., Hagelin, J. S., Nanopoulos, D. V., Olive, K., & Srednicki, M. (1984). Supersymmetric relics from the Big Bang. *Nuclear Physics B*, *238*, 453–476.

Enßlin, T. A., Biermann, P. L., Klein, U., & Kohle, S. (1998). Cluster radio relics as a tracer of shock waves of the large-scale structure formation. *Astronomy and Astrophysics*, *332*, 395–409.

Esmaili, A., Khatibi, S., & Najafabadi, M. M. (2017). Constraining the monochromatic gamma-rays from dark matter annihilation by the LHC. *Physical Review D: Particles and Fields*, *96*, 015027.

Farnsworth, D., Rudnick, L., Brown, S., & Brunetti, G. (2013). Discovery of megaparsec-scale, low surface brightness nonthermal emission in merging galaxy clusters using the Green Bank Telescope. *Astrophysical Journal*, *779*, 189.

Feretti, L., Giovannini, G., Govoni, F., & Murgia, M. (2012). Cluster of galaxies: observational properties of the diffuse radio emission. *Astronomy and Astrophysics Review*, *20*, 54.

Finoguenov, A., Sarazin, C. L., Nakazawa, K., Wik, D. R., & Clarke, T. E. (2010). XMM-Newton observation of the northwest radio relic region in A3667. *Astrophysical Journal*, *715*, 1143–1151.

Fixsen, D. J. (2009). The temperature of the cosmic microwave background. *Astrophysical Journal*, *707*, 916–920.

Fornengo, N., Maccione, L., & Vittino, A. (2014). Constraints on particle dark matter from cosmic-ray antiprotrons. *Journal of Cosmology and Astroparticle Physics*, *2004*, 003.

Fox, P. J., Harnik, R., Kopp, J., & Tsai, Y. (2011). LEP shines light on dark matter. *Physical Review D: Particles and Fields*, *84*, 014028.

Ghisellini, G., Guilbert, P. W., & Svensson, R. (1988). The synchrotron boiler. *Astrophysical Journal*, *334*, L5–L8.

Giacintucci, S., Markevitch, M., Venturi, T., Clarke, T. E., Cassano, R., & Mazzotta, P. (2014). New detections of radio minihalos in cool cores of galaxy clusters. *Astrophysical Journal*, *781*, 9.

Giovannini, G., Bonafede, A., Feretti, L., Govoni, F., Murgia, M., Ferrari, F., & Monti, G. (2009). Radio halos in nearby (z<0.4) clusters of galaxies. *Astronomy and Astrophysics*, *507*, 1257–1270.

Gitti, M., Brunetti, G., & Setti, G. (2002). Modeling the interaction between ICM and relativistic plasma in cooling flows: The case of the Perseus cluster. *Astronomy and Astrophysics*, *386*, 456–463.

Goldberg, H. (1983). Constraint on the photino mass from cosmology. *Physical Review Letters*, *50*, 1419–1422.

Gondolo, P., Edsjö, J., Ullio, P., Bergström, L., Schelke, M., & Baltz, E. A. (2004). DarkSUSY: Computing supersymmetric dark matter properties numerically. *Journal of Cosmology and Astroparticle Physics*, *2004*(07), 008.

Gondolo, P., Edsjö, J., Ullio, P., Bergström, L., Schelke, M., Baltz, E. A., ... Duda, G. (2015, April). *DarkSUSY Home Page.* Retrieved from http://www.darksusy.org

Groener, A. M., Goldberg, D. M., & Sereno, M. (2016). The galaxy cluster concentration-mass scaling relation. *Monthly Notices of the Royal Astronomical Society*, *455*, 892–919.

Hooper, D., & Goodenough, L. (2011). Dark matter annihilation in the Galactic Center as seen by the Fermi Gamma Ray Space Telescope. *Physics Letters B*, *697*, 412–428.

Hooper, D., & Profumo, S. (2007). Dark matter and collider phenomenology of universal extra dimensions. *Physics Reports*, *453*, 29–115.

Hubble, E. (1929). A relation between distance and radial velocity among extra-galactic nebulae. *Proceedings of the National Academy of Science*, *15*, 168–173.

Hudson, D. S., Mittal, R., Reiprich, T. H., Nulsen, P. E. J., Andernach, H., & Sarazin, C. L. (2010). What is a cool-core cluster? a detailed analysis of the cores of the X-ray flux-limited HIFLUGCS cluster sample. *Astronomy and Astrophysics*, *513*, A37.

IceCube Collaboration. (2016). All-flavour search for neutrinos from dark matter annihilations in the Milky Way with IceCube/DeepCore. *The European Physical Journal C*, *76*, 531.

Jungman, G., Kamionkowski, M., & Griest, K. (1996). Supersymmetric dark matter. *Physics Reports*, *267*, 195–373.

Kale, R., Venturi, T., Giacintucci, S., Dallacasa, D., Cassano, R., Brunetti, G., . . . Athreya, R. (2015). The Extended GMRT Radio Halo Survey. II. Further results and analysis of the full sample. *Astronomy and Astrophysics*, *579*, A92.

Klein, O. (1926). Quantum theory and five-dimensional theory of relativity. *Zeitschrift für Physik*, *37*, 895–906.

Klypin, A. A., Trujillo-Gomez, S., & Primack, J. (2011). Dark matter halos in the standard cosmological model: Results from the Bolshoi simulation. *Astrophysical Journal*, *740*, 102.

Kravtsov, A. V., Klypin, A. A., Bullock, J. S., & Primack, J. R. (1998). The cores of dark matter-dominated galaxies: theory versus observations. *Astrophysical Journal*, *502*, 48–58.

Kuchar, P., & Enßlin, T. A. (2011). Magnetic power spectra from Faraday rotation maps. REALMAF and its use on Hydra A. *Astronomy and Astrophysics*, *529*, A13.

Kuo, P.-H., Hwang, C.-Y., & Ip, W.-H. (2004). The evolution of diffuse radio sources in galaxy clusters. *Astrophysical Journal*, *604*, 108–115.

Łokas, E. L., Wojtak, R., Gottlöber, S., Mamon, G. A., & Prada, F. (2006). Mass distribution in nearby Abell clusters. *Monthly Notices of the Royal Astronomical Society*, *367*, 1463–1472.

Longair, M. S. (2011). *High energy astrophysics* (3rd ed.). New York: Cambridge University Press.

LUX Collaboration. (2016). Results on the spin-dependent scattering of weakly interacting massive particles on nucleons from the Run 3 data of the LUX experiment. *Physical Review Letters*, *116*, 161302.

Marchegiani, P., & Colafrancesco, S. (2016). The role of dark matter sub-halos in the non-thermal emission of galaxy clusters. *Journal of Cosmology and Astroparticle Physics*, *2016*(11), 033.

Mazzotta, P., & Giacintucci, S. (2008). Do radio core-halos and cold fronts in non-major-merging clusters originate from the same gas sloshing? *Astrophysical Journal*, *675*, L9–L12.

Miniati, F., Jones, T. W., Kang, H., & Ryu, D. (2001). Cosmic-ray electrons in groups and clusters of galaxies: Primary and secondary populations from a numerical cosmological simulation. *Astrophysical Journal*, *562*, 233–253.

Moore, B., Quinn, T., Governato, F., Stadel, J., & Lake, G. (1999). Cold collapse and the core catastrophe. *Monthly Notices of the Royal Astronomical Society*, *310*, 1147–1152.

Navarro, J. F., Frenk, C. S., & White, S. D. M. (1997). A universal density profile from hierarchical clustering. *Astrophysical Journal*, *490*, 493–508.

Navarro, J. F., Hayashi, E., Power, C., Jenkins, A. R., Frenk, C. S., White, S. D. M., ... Quinn, T. R. (2004). The inner structure of ΛCDM haloes - III. Universality and asymptotic slopes. *Monthly Notices of the Royal Astronomical Society*, *349*, 1039–1051.

Patrignani et al. (Particle Data Group). (2016). Review of particle physics. *Chinese Physics C*, *40*(10), 100001.

Peccei, R. D., & Quinn, H. R. (1977). CP conservation in the presence of pseudoparticles. *Physical Review Letters*, *38*, 1440–1443.

Petrosian, V. (2001). On the nonthermal emission and acceleration of electrons in Coma and other clusters of galaxies. *Astrophysical Journal*, *557*, 560–572.

PICO Collaboration. (2016). Improved dark matter search results from PICO-2L Run 2. *Physical Review D: Particles and Fields*, *93*, 061101.

Planck Collaboration. (2016). Planck 2015 results. XIII. Cosmological parameters. *Astronomy and Astrophysics*, *594*, A13.

Prada, F., Klypin, A. A., Cuesta, A. J., Betancort-Rijo, J. E., & Primack, J. (2012). Halo concentrations in the standard Λ cold dark matter cosmology. *Monthly Notices of the Royal Astronomical Society*, *423*, 3018–3030.

Profumo, S. (2012). Dissecting cosmic-ray electron-positron data with Occam's razor: the role of known pulsars. *Central European Journal of Physics*, *10*, 1–31.

Rines, K., & Diaferio, A. (2006). CIRS: Cluster Infall Regions in the Sloan Digital Sky Survey. I. Infall patterns and mass profiles. *The Astronomical Journal*, *132*, 1275–1297.

Rines, K., Geller, M. J., Kurtz, M. J., & Diaferio, A. (2003). CAIRNS: The cluster and infall region nearby survey. I. redshifts and mass profiles. *The Astronomical Journal*, *126*, 2152–2170.

Rudnick, L., & Lemmerman, J. A. (2009). An objective survey of Mpc-scale radio emission in $0.03<z<0.3$ bright X-ray clusters. *Astrophysical Journal*, *697*, 1341–1357.

Sarazin, C. L. (1999). The energy spectrum of primary cosmic-ray electrons in clusters of galaxies and inverse Compton emission. *Astrophysical Journal*, *520*, 529–547.

Servant, G., & Tait, T. M. P. (2003). Is the lightest Kaluza-Klein particle a viable dark matter candidate? *Nuclear Physics B*, *650*, 391–419.

Slipher, V. M. (1917). Nebulae. *Proceedings of the American Philosophical Society*, *56*, 403–409.

Solovyeva, L., Anokhin, S., Feretti, L., Sauvageot, J. L., Teyssier, R., Giovannini, G., . . . Neumann, D. (2008). The dynamical state of A548 from XMM-Newton data: X-ray and radio connection. *Astronomy and Astrophysics*, *484*, 621–630.

Springel, V., Wang, J., Vogelsberger, M., Ludlow, A., Jenkins, A., Helmi, A., . . . White, S. D. M. (2008). The Aquarius Project: the subhaloes of galactic haloes. *Monthly Notices of the Royal Astronomical Society*, *391*, 1685–1711.

Storm, E., Jeltema, T. E., Profumo, S., & Rudnick, L. (2013). Constraints on dark matter annihilation in clusters of galaxies from diffuse radio emission. *Astrophysical Journal*, *768*, 106.

Super-Kamiokande Collaboration. (2011). An indirect search for weakly interacting massive particles in the Sun using 3109.6 days of upward-going muons in Super-Kamiokande. *Astrophysical Journal*, *742*, 78.

Taylor, G. B., Fabian, A. C., & Allen, S. W. (2002). Magnetic fields in the Centaurus cluster. *Monthly Notices of the Royal Astronomical Society*, *334*, 769–776.

Vacca, V., Murgia, M., Govoni, F., Feretti, L., Giovannini, G., Perley, R. A., & Taylor, G. B. (2012). The intracluster magnetic field power spectrum in A2199. *Astronomy and Astrophysics*, *540*, A38.

van Weeren, R. J., Röttgering, H. J. A., Brüggen, M., & Hoeft, M. (2010). Particle acceleration on Megaparsec scales in a merging galaxy cluster. *Science*, *330*, 347–349.

van Albada, T. S., Bahcall, J. N., Begeman, K., & Sanscisi, R. (1985). Distribution of dark matter in the spiral galaxy NGC 3198. *Astrophysical Journal*, *295*, 305–313.

Venturi, T., Giacintucci, S., Dallacasa, D., Cassano, R., Brunetti, G., Bardelli, S., & Setti, G. (2008). GMRT radio halo survey in galaxy clusters at z = 0.2-0.4. II. The eBCS clusters and analysis of the complete sample. *Astronomy and Astrophysics*, *484*, 327–340.

Venturi, T., Giovannini, G., & Feretti, L. (1990). High-sensitivity radio observations of the Coma cluster of galaxies. *The Astronomical Journal*, *99*, 1381–1396.

Voigt, L. M., & Fabian, A. C. (2006). Galaxy cluster mass profiles. *Monthly Notices of the Royal Astronomical Society*, *368*, 518–533.

Weinberg, S. (1978). A new light boson? *Physical Review Letters*, *40*, 223–226.

Wilczek, F. (1978). Problem of strong P and T invariance in the presence of instantons. *Physical Review Letters*, *40*, 279–282.

XENON100 Collaboration. (2013). Limits on spin-dependent WIMP-nucleon cross sections from 225 live days of XENON100 data. *Physical Review Letters*, *111*, 021301.

Zwicky, F. (1933). The redshift of extragalactic nebulae. *Helvetica Physica Acta*, *6*, 110–127.

LIST OF PUBLICATIONS AND PAPERS PRESENTED

1. **Kiew, C.-Y.**, Hwang, C.-Y., & Abidin, Z. Z. (2017). Constraints on the dark matter neutralinos from the radio emissions of galaxy clusters. *Monthly Notices of the Royal Astronomical Society*, *467*, 2924–2933.